

AN OVERVIEW OF RESULTS FROM THE ION DIAGNOSTICS SENSORS FLOWN ON DS1*

D. E. Brinza, M. D. Henry, A. T. Mactutis, K. P. McCarty, J. D. Rademacher,
T. R. van Zandt, P. Narvaez, J. J. Wang and B. T. Tsurutani
Jet Propulsion Laboratory, California Institute of Technology, Pasadena, California

I. Katz and V. A. Davis
Maxwell Technologies, San Diego, California

S. Moses
TRW, One Space Park, Redondo Beach, California

G. Musmann, F. Kuhnke, I. Richter, C. Othmer, K.-H. Glassmeier
Institute for Geophysics and Meteorology, Technical University of Braunschweig, Braunschweig, Germany

ABSTRACT

The Deep Space 1 (DS1) mission has successfully validated the use of ion propulsion technology for interplanetary spacecraft. The NASA Solar Electric Propulsion (SEP) Technology Applications Readiness (NSTAR) Project developed the Ion Propulsion Subsystem (IPS) for DS1. As part of the NSTAR validation effort, the NSTAR Project included a diagnostics element to characterize the local environment produced during IPS operations and its effects on spacecraft subsystems and science instruments. An integrated, comprehensive set of diagnostics, the NSTAR Diagnostics Package (NDP) was developed and operated on DS1 to characterize the IPS environment. The DS1 Spacecraft Team officially assigned the name "IPS Diagnostics Subsystem (IDS)" to the NDP for the DS1 mission. During the technology validation phase of the DS1 mission, a large amount of data was collected from the IDS under a variety of IPS operating conditions. IDS was able to characterize the contamination environment, charge-exchange xenon ion and electron population and energies, plasma noise and electromagnetic noise, and magnetic fields associated with IPS. The results presented here describe the charge-exchange plasma, contamination, plasma wave/EMI, and DC magnetic environments critical to designers of future space missions using ion propulsion.

INTRODUCTION

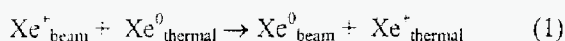
This introduction is intended to provide the reader with a brief overview of Ion Propulsion Subsystem (IPS) environmental perturbations considered important for spacecraft and science operations. The objective for the IPS Diagnostics Subsystem (IDS) flown on Deep Space 1 (DS1) is to characterize these environments within significant resource constraints. The technical requirements for IDS measurements are based upon the results from the NASA/USAF Workshop on Environmental Diagnostics for ELITE/STAR¹.

The NASA Solar Electric Propulsion (SEP) Technology Applications Readiness (NSTAR) ion thruster operating aboard DS1 generates a local environment that includes electrostatic, magnetic and electromagnetic fields, charged particles, and neutral particles. The thruster environmental components, in combination with the natural space environment and the space vehicle, produce the "induced environment." The induced environment has the potential of impacting the performance of spacecraft subsystems or science sensors. Based on the operating experience thus far on DS1, the IPS induced environment is benign to spacecraft subsystems.

Plasma Environment

The operation of the ion thruster with neutralizer generates a plasma flow about the spacecraft². The primary beam (1 kV) xenon ions interact with thermal energy xenon atoms diffusing from the thruster via a resonant charge exchange process to generate low-energy ions in the plume:

Copyright © 2001 by the American Institute of Aeronautics and Astronautics, Inc. ~~No copyright is asserted in the United States under Title 17, U.S. Code. The U.S. Government has a royalty-free license to exercise all rights under the copyright claimed herein for Governmental Purposes. All other rights are reserved by the copyright owner.~~ *Step*



The total charge-exchange ion current generated is estimated to be less than 5 mA for the NSTAR thruster. These charge-exchange ions are accelerated by electric field gradients in the vicinity of the thruster, moving radially at energies up to 20 eV. Electrons are emitted from a hollow cathode neutralizer similar in design to the plasma contactor to be used on the International Space Station. The electrons from the neutralizer associate with the charge-exchange ions to create a cold, flowing plasma. This cold, flowing plasma effects the spacecraft in ways described in the paragraphs that follow.

Spacecraft Potential—Thruster operation might be expected to “clamp” the spacecraft potential to the local space plasma potential. The electron temperature (expected to be 1 to 3 eV) is anticipated to drive the spacecraft potential³ to no more than -10 V. In the interplanetary environment, the Debye length is typically greater than 10 m; thus, direct measurement of spacecraft potential cannot be performed by Langmuir probe sensors. Electron temperature measurements, coupled with ion current and energy knowledge, and a reliable ion plasma-plume modeling tool are used to estimate the spacecraft potential.

Current Balance—The plasma flow produced by the thruster can provide a path for parasitic current loss from the solar arrays⁴. The extent of this current drain is determined by solar array design, spacecraft ground convention, solar array potential, and the plasma densities associated with the thruster. The currents from the solar array, through the ion thruster system, and the spacecraft bus were monitored as part of the DS1 engineering measurements. Analyses of these measurements are required to understand current balance within the spacecraft. The NSTAR IPS has an internal ground (neutralizer common) that is virtually isolated from the DS1 spacecraft ground. Potential measurements of the neutralizer common with respect to spacecraft ground provide information regarding current flow between the IPS and DS1. Effects of Langmuir Probe operation on IPS neutralizer common provide additional insight into current balance on DS1 during IPS operations.

Charge-Exchange Ion Interference—The density of charge-exchange ions from the NSTAR ion engine can present a risk to sensitive particle-detection instruments. Mass spectrometers designed to operate in solar-wind environments are typically particle-counting instruments with high-gain channel electron multipliers or other sensitive detectors. Measurements of the charge-exchange ion flux near the NSTAR engine is made with a retarding potential analyzer. The Plasma Experiment for Planetary Environments (PEPE) particle spectrometer measures

electron and charge-exchange ion densities on the opposite side of the DS1 spacecraft.

Energetic Ion Impingement—The ion plume contains energetic ions (up to 1 keV) that would erode surfaces exposed to direct impingement via sputtering. These ions are emitted from the thruster primarily (95%) in a cone with a half angle of about 45° about the thrust axis. Measurable energetic ion flux at higher off-axis angles may be found; however, their risk to spacecraft subsystems is low. Charge exchange ions may also sputter coatings; however, a current of less than 1 $\mu\text{A}/\text{cm}^2$ of low-energy ions (<20 eV) is expected at 75-cm distance from the thruster (at the exit plane). This charge-exchange ion flux is not expected to sputter material from spacecraft surfaces. Ground measurements of erosion (and contamination) were performed for long-duration tests. Flight measurements include a retarding potential analyzer with sub-nA sensitivity and bias voltages up to +100 VDC.

Contamination Environment

The xenon propellant used in the NSTAR thruster is a non-contaminating species. One of the wear mechanisms for the thruster involves gradual sputtering of the molybdenum accelerator grids, eventually leading to mechanical failure of the grid structure⁵. Sputtered neutral molybdenum atoms are emitted in the general direction of the plume. Charge-exchange of the sputtered molybdenum with primary ion beams will occur (albeit with much smaller cross section than for resonant charge exchange of xenon). The charge-exchange molybdenum ions may be transported to surfaces “upstream” of the thruster. The upstream deposition rates are expected to be very low, even in the immediate vicinity of the thruster. However, even very thin coatings on the order of a few Angstroms (\AA , $1\text{\AA} = 10^{-10}\text{ m}$) can produce significant effects in thermo-optical (solar absorptance and emittance) properties of thermal control materials or transmission of solar radiation through solar cell cover glasses.

The results from contamination sensors are useful from two perspectives: (1) The in-flight data provides a spacecraft systems engineer information for modeling environments on future spacecraft and (2) the data, when correlated with ground test, can help assess engine health. Contamination measurements can provide an indication of grid wear. The flight measurement will rely upon a calorimetric measurement of thermo-optical properties of a space-stable optical solar reflector supplemented with rate measurements via a quartz crystal microbalance (QCM).

Fields Environment

The NSTAR thruster produces static electric and magnetic fields and electromagnetic disturbances during routine operation. The design of the thruster, neutralizer, and power processor unit (PPU) considers the conducted and emitted electromagnetic interference (EMI) effects. The interaction of the plume and charge exchange plasma with the natural environment and spacecraft power system can also generate electrostatic, magnetic, and electromagnetic fields. The following sections describe electric, magnetic, and electromagnetic fields effects induced by the NSTAR IPS on DS1.

Electrostatic Fields—Charge-exchange plasma associated with the NSTAR engine provides a conductive medium for time-varying electrostatic fields⁶. Plasma waves are generated in the region of the neutralizer by temporal instabilities in the hollow cathode discharge. The electron plasma frequency (ν) varies with the square root of electron density (n_e)⁷:

$$\nu \approx 8.98 \text{ (Hz} \cdot \text{m}^{3/2}) n_e^{1/2} \quad (2)$$

The plasma density is expected to decrease from $10^{15}/\text{m}^3$ in the plume just outside the thruster to less than $10^{13}/\text{m}^3$ at one meter from the engine. Plasma waves have been measured for ion thrusters from very low frequencies (a few kilohertz) up to tens of megahertz. Due to locally strong magnetic fields, the plume is also a source of cyclotron electric fields. Flight measurements with an electric field antenna sensitive over the frequency range of 10 Hz to 30 MHz and a search-coil magnetometer from 10 Hz to 50 kHz are performed aboard DS1.

Electromagnetic Fields—The primary electromagnetic interference (EMI) concern with an IPS is its impact on the spacecraft communications system. In interplanetary missions, attenuation and phase delay due to the plume/plasma density may occur along the link path. Measurements in ground test have provided data for effective modeling of plume effects on RF electromagnetic wave propagation. Flight measurements utilizing the on-board telecommunications system were performed on DS1. The DS1 Mission Operations Team incorporated maneuvers with telecom operations to provide through-the-plume geometry for assessment of worst-case effects of ion thruster operations with spacecraft communications. No detectable change in telecom signal strength could be observed in this measurement.

High-level electromagnetic fields may arise from thruster operation from current fluctuations in the NSTAR propulsion system. The PPU was subjected to electromagnetic compatibility testing (such as RE101 from MIL-STD-461D) with the unit operating with a characteristic

thruster load. Strong AC fields can impact scientific instruments and possibly spacecraft subsystems. AC fields from the IPS will interfere with fields measurements; therefore, science fields measurements should be made only while the IPS is not thrusting. The space science community has interest in lower frequency EMI characteristics of ion propulsion system operations. Thrust-phase portions of the mission may limit particles and fields measurements. It was expected that the thruster beam would produce waves due to beam instabilities induced by the ambient environment. The search-coil magnetometer detects EMI over the frequency range of 10 Hz to 50 kHz; however, signals due to ion-beam solar wind have not been uniquely identified. Other EMI sources, such as the engine gimbal assembly (EGA), and solar array actuators have been detected on DS1.

Magnetic Fields—DC magnetic fields arise from permanent magnets used in the thruster design. The permanent magnets in the ion thruster are configured to maximize ionization efficiency⁸. The thruster body is constructed of titanium; therefore, DC magnetic fields surround the thruster. Measurements of the magnetic field pattern for the NSTAR ion engine indicate fields of nearly 5000 nT are expected at one meter from the thruster. Electrical currents through the spacecraft power system and ion propulsion system produce other stray magnetic fields. DC fields are a significant consideration in science missions where the magnetic fields are measured with high sensitivity. In a typical science mission, magnetometers are generally exposed to DC fields due to the spacecraft subsystems of less than 1 nT. For the DS1 technology validation mission, magnetic cleanliness of the spacecraft was not a major consideration. The DC magnetic fields measured on DS1 contains contributions from the NSTAR IPS and the rest of the DS1 spacecraft (heaters, solar arrays, other subsystems). As a goal, the flight magnetic measurements are intended to distinguish spacecraft fields from thruster-generated fields with better than 1-nT sensitivity.

DIAGNOSTICS ELEMENT DESCRIPTION

The NSTAR diagnostics effort includes ground test, modeling, and flight measurements to assess the environmental impact of ion-thruster operations on spacecraft payloads (instruments) and sub-systems. The validation of performance of the ion thruster sub-system includes direct measurement of phenomenology associated with the interactions described in the introduction. The ground test, modeling, and flight measurement approaches are described below.

Ground Test Diagnostics

The NSTAR thruster element included development and test of engineering model thruster (EMT) and flight thruster systems. The NSTAR contractor, Hughes Electron Dynamics Division, delivered flight thrusters with significant design heritage to the 30-cm xenon ion thrusters developed by the NASA Glenn Research Center⁹. Various ground tests were conducted throughout the NSTAR project, culminating with flight thruster compatibility tests with the DS1 spacecraft prior to launch. The following sections describe these NSTAR tests in the context of diagnostic measurements.

Early EMT Testing—The early EMT tests were moderate in duration (hundreds of hours up to 2000 hr) to characterize erosion characteristics, thruster performance, etc. During this phase, design details and operating points of the NSTAR thruster were adjusted to enhance thruster reliability and performance for long duration operation. Since minor changes to thruster design may substantially alter the contamination, EMI, or plasma conditions associated with the thruster, very few quantitative diagnostic tests were planned. A few witness materials were examined and qualitative measurements of EMI were performed; however, these tests remain geared to thruster evaluation.

Life Demonstration Test—The NSTAR program performed a life demonstration test (LDT) of an ion engine that successfully demonstrated the ability of the NSTAR EMT to operate at full power for more than 8000 hours¹⁰. The LDT afforded an excellent opportunity to collect contamination data and to establish flight plasma sensor design and performance requirements. Ground tests produced "chamber effects" that can interfere with the measurement of the relevant environments, interaction measurements; however, there were mitigation approaches that provided useful data. Much of the data gathered from the LDT was of comparative nature: before and after grid mass, thrust vector stability, engine efficiency, etc. The NSTAR diagnostics element characterized the magnitude and stability of the DC magnetic field produced by the EMT before and after the LDT.

Contamination measurements in the LDT were considered valuable since the magnitude of erosion and deposition measurements scale with operating times, especially for witness specimen measurements. The NSTAR diagnostic element performed a contamination assessment during the LDT to quantify deposition amounts and/or erosion effects while providing an estimate of the contribution of chamber effects. "Collimated" witness specimens (fused silica windows) were located at various angles with respect to the plume axis. "Un-collimated" witness specimens were mounted

in equivalent location to assess chamber effects. The post-LDT analyses determined composition of deposits as well as the thickness as a function of angle from the beam.

The LDT provided the opportunity to perform periodic plasma probe tests, including Langmuir probe, plasma wave antenna, retarding potential analysis, and even ion/neutral mass spectrometry. Simple model sensors were installed within the LDT test chamber, with major consideration given to minimizing risk to the thruster or the facility. The NSTAR Project would not accept significant technical nor schedule risk from diagnostics in the execution of the LDT.

EMI/EMC—As part of the acceptance process, the flight units underwent characterization of DC magnetic fields, measurement of DC and AC magnetic fields during operation, measurement of AC electric fields during operation, and assessment of plume effect on RF communications. These tests were performed at JPL and at the NASA Glenn Research Center. Included in this test was a spacecraft-level test in which the NSTAR PPU was operated into a resistive load.

DS1 IPS Compatibility Test—The full flight system functional test of the IPS on DS1 was conducted in vacuum following spacecraft thermal vacuum testing. This test also provided an opportunity to characterize plasma and electric/magnetic fields associated with operation of the ion thruster in flight configuration. IDS hardware was integrated and fully operational for the IPS compatibility test. Although the IPS operating time was limited, IDS successfully captured plasma and fields data in this test. Correlation with flight data provides insight into chamber effects on potential and EMI measurements.

Modeling Tools

The NSTAR Project has invested significant effort in developing plume models to predict local environments on spacecraft utilizing ion propulsion. These models were used extensively to aid in establishing measurement requirements for the IPS Diagnostics Subsystem. Results from analysis of the IDS flight data will be compared with model predictions to update the modeling tools.

Direct Simulation Techniques—Monte-Carlo particle-in-cell (PIC) codes¹¹ were developed and executed for electrostatic and electromagnetic characteristics of the NSTAR ion thruster in various environments (free-space, chamber, DS1 spacecraft with simple boundary conditions). The computations simulate plumes due to the NSTAR ion engine using accurate characteristics for engine operations (primary-beam voltage, current, and spatial distributions, propellant utilization, neutralizer conditions, etc.). The generation and propagation of

charge-exchange ions are based on a purely physical model that includes particle densities and velocities, accurate collision cross sections, and Coulombic and Lorentz forces. These codes were hosted on massively parallel processors to allow statistically meaningful simulations to be performed in reasonable amounts of time. The characteristics of the charge-exchange ion flow were useful to determine the orientation of the NSTAR diagnostic sensors and to estimate the anticipated magnitudes of charge-exchange currents, plasma densities, and temperatures.

Semi-empirical Modeling—The Environment Work Bench (EWB) modeling tool developed at Maxwell Technologies was employed for estimating system-level interactions associated with the NSTAR ion engine operating on the DS1 spacecraft¹². The ion engine plume model used in EWB was initially based on laboratory data and PIC code simulations of the NSTAR ion engine. The plume model will be updated with refined modeling and flight data results in order to provide a useful tool for design of future ion propulsion based missions. In the future, systems engineers, mission planners, and principal investigators can utilize this system-level modeling tool on conventional (desktop or laptop) computers.

IPS Diagnostics Subsystem on DS1

A suite of 12 diagnostic sensors was integrated into the IDS shown in Figure 1. IDS was located adjacent to the NSTAR ion engine on the DS1 spacecraft.

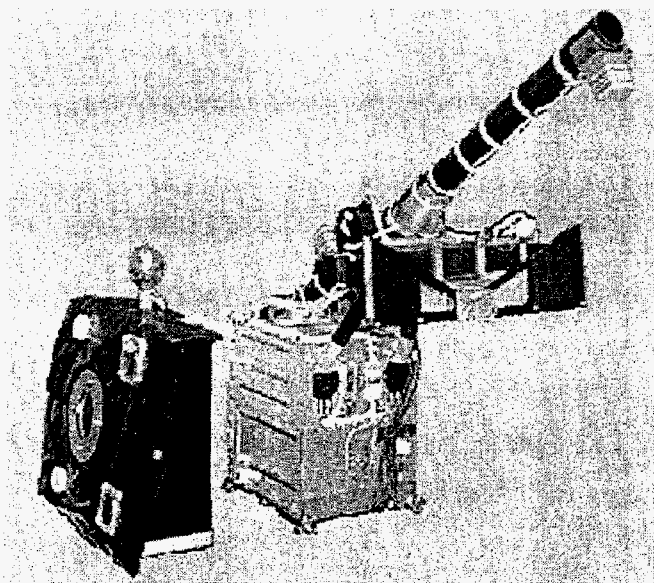


Figure 1. IPS Diagnostics Subsystem hardware

IDS Architecture—IDS consists of two interconnected hardware units: the Diagnostics Sensors Electronics Unit (DSEU) and the Remote Sensors Unit (RSU). The DSEU

component of the IDS has considerable heritage to SAMMES, a modular instrument architecture developed by BMDO^{13,14}. A block diagram for the IDS is shown in Figure 2. The IDS is a highly integrated instrument package with a single +28 VDC power and dual MIL-STD-1553 serial communications interface to the DS1 spacecraft. The compact IDS instrumentation package weighed just 8 kg and required 21 W for full operation.

The IDS contains two separate processor elements: the DSEU microprocessor and the fields measurement processor (FMP)¹⁵. The DSEU microprocessor supports the communications interface with DS1, controls serial communications with the FMP, and digitizes and controls the sensors within the RSU. The IDS operates as a remote terminal on the DS1 MIL-STD-1553 serial bus. Telemetry from the RSU sensors is collected on 2-second intervals and placed in selected 1553 subaddresses for transmission to DS1. Configuration messages are transmitted to the DSEU to select active sensors within the RSU and FMP and to establish sweep ranges and gains for these sensors. Configuration messages to the FMP are passed through the DSEU to the FMP directly. The DSEU polls the FMP for data at half-second intervals. In the typical FMP "scan" mode operation, a block of sensor data is transmitted at 16-second intervals. Occasionally, the FMP will transmit 1-second waveforms sampled at 20 kHz from the plasma wave and search sensors and 20 Hz from the flux-gate magnetometers. These "burst" events can be commanded or initiated via internal triggering within the FMP.

The highly integrated architecture greatly simplified spacecraft interface design, integration, and mission operations for IDS. The interface control document was developed in a very straightforward process with the greatest issue involving positioning of the IDS hardware to avoid interferences with the launch vehicle upper stage. Mechanical and electrical integration of IDS was accomplished within 2 hours. Mode changes during mission operations was accomplished by transmitting single 1553 messages (64-byte) at the desired time. These commands were readily integrated into operations sequences.

Contamination Monitors—Two QCM and calorimeter pairs were integrated in the RSU to characterize mass-deposition rates and contamination effects on surface thermo-optical properties. One pair of sensors is oriented to a direct line-of-sight view of the NSTAR ion engine. The DS1 propulsion module shadows the other contamination monitor pair from direct view of the NSTAR engine. The QCMs detect mass variations on the sensor surface via the induced frequency change in the oscillating-quartz crystal sensor. The calorimeters provide indirect knowledge of solar absorptance and

hemispherical emittance by temperature measurement of the thermally isolated sensor surface.

Each QCM (Mark 16 flight sensors procured from QCM Research, Laguna Beach, California) provides very high sensitivity measurement ($<10 \text{ ng/cm}^2$) of mass accumulation on the sensor¹⁶. The long-term drift of the QCM should not exceed 50 ng/cm^2 per month, which corresponds to a minimum detectable molybdenum deposit rate of one monolayer per year. Temperature changes and solar illumination of the sense crystal affect QCM response. For substantial mass accumulation, the temperature and solar illumination effects on the QCM measurement are minor.

The calorimeters¹⁷ can determine solar absorptance changes to better than 0.01 and emissivity changes to better than 0.01. The calorimeters use the Sun as a stimulus for determination of solar absorptance. The calorimeters include a controlled heater to permit measurement of the hemispherical emissivity of the surface. Spacecraft surfaces in the field of view of the calorimeter complicate data analysis because of the

uncertain heat loads that these surfaces provide to the sensor surface.

The data from the QCM and calorimeter sensors are reduced, analyzed, and correlated with NSTAR ion engine operations. The QCM with direct line-of-sight to the NSTAR ion engine was expected to accumulate readily detectable amounts of sputtered molybdenum. Pre-flight estimates indicated the deposition rate on non-line-of-sight surfaces near the thruster from ionized molybdenum will be very low.

Charge Exchange Plasma Sensors—IDS includes a retarding potential analyzer (RPA) and two Langmuir probes to characterize the charge-exchange plasma produced by the NSTAR thruster. The RPA measures the charge-exchange ion energy distribution over the range of 0 to +100 eV near the thruster exit plane. The RPA sensor axis is co-aligned with the predicted charge-exchange ion flow direction expected at the RPA location. Langmuir probes are used to measure the electron temperature and the density of the plasma near the NSTAR thruster.

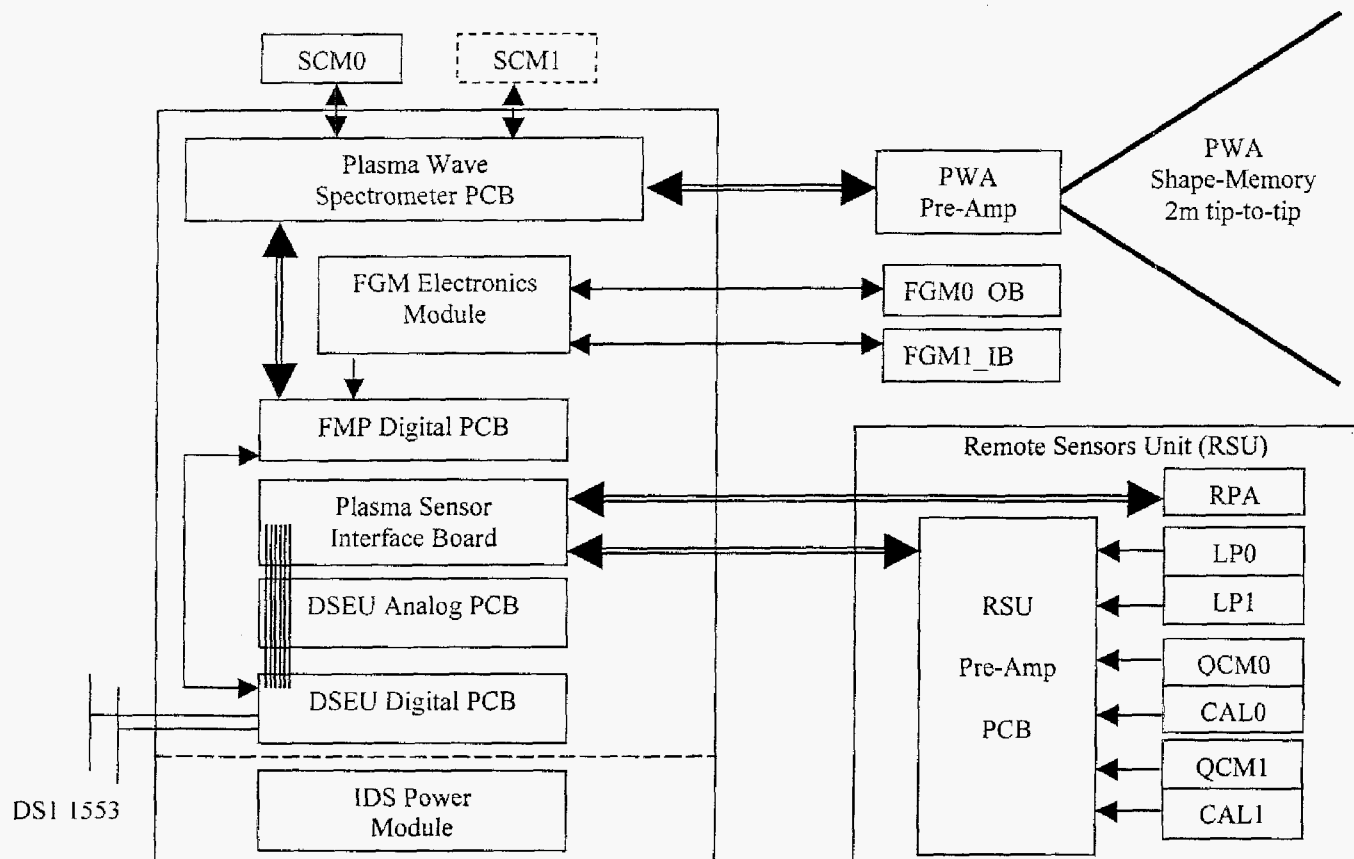


Figure 2. IPS Diagnostics Subsystem block diagram

The RPA used in the IDS was salvaged from the Ion Auxiliary Propulsion System on P80-1 (Teal Ruby). These units were fabricated and qualified for flight by Hughes Electronics in 1978¹⁸. Extensive performance and calibration data have been obtained for the flight units. The RPA is a four-grid design with screen and suppressor grids operated at -12 VDC and the bias-grid voltage adjustable from 0 to +100 VDC. An RPA sweep consists of sixteen voltage steps, within the 0 to +100-V range, with a minimum step size of 0.39 V. The currents for the biasing voltages applied to the grids within the RPA will be monitored and included in the RPA telemetry stream to permit detailed analysis of the charge-exchange plasma near the engine. The ion collector includes a pre-amplifier with selectable full-scale detection ranges from 10^{-9} to 10^{-3} A. In the case of the IDS, the full-scale selectable gains for the RPA are 10 nA, 1 μ A, 10 μ A, and 100 μ A. The entrance aperture to the RPA is 5 cm in diameter.

Two Langmuir probe sensors were included in the IDS: LP0, a spherical probe (4-cm diameter), and LP1, planar ring (50 cm²) on a conductive MLI blanket. The probes were independently biased (swept or constant voltage range) from -7 VDC to +11 VDC. Langmuir probe current measurement range extends from -500 μ A to +40 mA. The Langmuir probe-support circuitry was designed and fabricated by Sentran Corporation, Goleta, California.

Fields Measurements—The baseline diagnostic sensor package for NSTAR did not include electric or magnetic field sensors. The presence of high-density-field permanent magnets in the NSTAR thruster warranted investigation as to the long-term stability of these fields. An augmentation to the IDS for fields measurement was made possible by the participation of Technical University of Braunschweig (TUB), TRW, and the Jet Propulsion Laboratory (JPL) Integrated Space Physics Instrument team. Measurement of the DC magnetic fields was performed by two three-axis flux-gate magnetometers, each mounted on a short boom extending from the spacecraft. Measurements of low frequency AC magnetic fields (10 Hz to 50 kHz) characterize the electromagnetic interference (EMI) produced by the engine. In addition, it was possible that electromagnetic waves induced by plasma stream instabilities within the plume and by plume interactions with the solar wind could be detected. Two search coil magnetometer sensors were mounted to the boom to measure these electromagnetic waves. The plasma wave environment produced by the thruster was expected to be similar for emissions that have been measured for the Space Station Plasma Contractor hollow cathode source. The emissions are very broadband, from essentially DC to about 10 MHz, with interference with spacecraft operations highly improbable. A 2-m tip-to-tip dipole antenna with adjustable gain pre-amplifier on the boom measured the plasma wave environment over the frequency range of 10 Hz to 30 MHz.

Flux-Gate Magnetometers—Two sensitive, three-axis flux-gate magnetometers designed and built by TUB were mounted on the boom near the NSTAR ion engine. The inboard magnetometer is located in a high-density-field region (9,000 nT). The outboard magnetometer was positioned to place the sensor in a somewhat weaker field (less than 3,000 nT). The magnetometer sensitivity is better than 1 nT with $\pm 25,000$ -nT full-scale range. The maximum sampling rate of the flux-gate magnetometers is 20 Hz.

Search Coil Magnetometers—Two single-axis search coil magnetometers were mounted on the boom. One search coil is a new technology miniaturized sensor developed in the JPL MicroDevices Laboratory that uses a field rebalance technique for measurement. The second search coil was a build-to-print of the Orbiting Geophysical Observatory (OGO-6) single-axis sensor manufactured by Space Instruments, Inc., Irvine, California. The second search coil sensor was apparently damaged at the launch site by large AC fields and was inoperable during the DS1 mission. Flight measurements were performed with a measurement bandwidth over 10 Hz to 50 kHz. The full-scale range at 200 Hz is 100 nT with a resolution of 1 pT. The AC magnetic fields were characterized as a discrete power spectrum with four measurement intervals per decade. The transient waveform for "events" was also captured with a sampling rate of 20 kHz for 1sec windows. The transient recorder utilized a circular buffer with a threshold trigger to capture events. The threshold parameters can be updated via ground command through the DS1 spacecraft.

Plasma Wave Antenna—A simply deployed dipole plasma wave antenna (PWA) with adjustable-gain pre-amplifier was mounted onto the boom. The PWA is a pair of low-mass Ni-Ti shape-memory alloy (SMA) metallic strips with a tip-to-tip separation of 2 m. The PWA deployment occurs upon exposure of the stowed SMA coiled ribbon to the Sun. Within 2 hours, the PWA antenna slowly extends to its deployed position. The PWA is connected to a low-noise preamplifier co-located on the boom that was designed and built by TRW, Redondo Beach, California. The amplified PWA output is processed by the plasma wave spectrometer (PWS), also designed and built by TRW, to provide a spectrum analysis in a low-frequency domain of 10 Hz to 100 kHz and a high-frequency domain of 100 kHz to 30MHz. The low-frequency domain is characterized by a voltage-swept band pass filter with a minimum of four measurements per decade with an amplitude range of 100 μ V/m to 1000 mV/m. The high-frequency domain is characterized with a minimum of four measurements per decade with the same amplitude range as the low-frequency domain. Transient waveform measurements are performed at a 20-kHz sampling rate with a 1-second circular buffer. Threshold parameters for trigger and downlink of transient waveforms are capable of being uploaded from the DS1 spacecraft.

CHARGE-EXCHANGE PLASMA

The electrostatic potential of the DS1 spacecraft with respect to the ambient space plasma is determined by current balance^{11,12}. Charge-exchange plasma from the NSTAR ion engine drives the current balance on the spacecraft. The amount of charge-exchange plasma produced by the NSTAR ion engine varies with the engine operating conditions. Electric probes, such as the IDS Langmuir probes, are capable of sinking large amounts of current. The perturbations by the IDS Langmuir probes can substantially effect the DS1 spacecraft potential. The following sections describe the current understanding of the spacecraft potential, charge-exchange ion variation with engine thrust level, and effects produced by the IDS Langmuir Probes.

DS1 Chassis Potential w/o Langmuir Probe Bias Voltage

At equilibrium, spacecraft chassis ground potential is determined by the fact that the net current to the exposed conductors (thruster-mask ring around engine, Langmuir probe with black Kapton on RPA box, see Figure 3) is zero. In the interplanetary space plasma environment, the Debye length is much larger than the spacecraft dimensions. The plasma density from the ion engine is many orders of magnitude larger than the space plasma. The following analysis assumes the charge-exchange ions collected are orbit limited, which may be a questionable assumption.

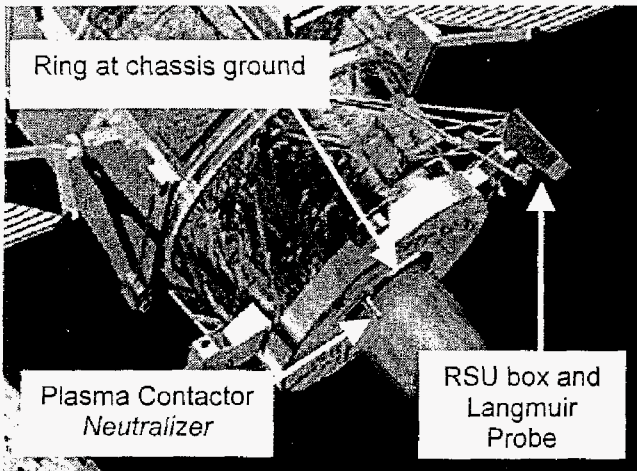


Figure 3. Major contributors to current balance on DS1

The surface area of the conductors and the plasma density at the conductor determines the relative contribution of current collection. The surface area of the thruster mask ring is 0.085 m² (inner radius 0.15 m, outer radius 0.2225 m). The surface area of the ring Langmuir probe is 0.0050 m², without considering the black Kapton outer blanket of the RSU. It will be shown later that the effective collection area is approximately double when the conductive black

Kapton is included. Plasma density estimates were computed via PIC code simulation^{11,12} (Figure 4). The plasma density at the thruster mask ring is in excess of 10¹⁴ m⁻³; the density at the RPA Langmuir probe is less than 10¹³ m⁻³. Current balance at the thruster-mask ring, therefore, dominates the chassis potential with no bias on the Langmuir probe.

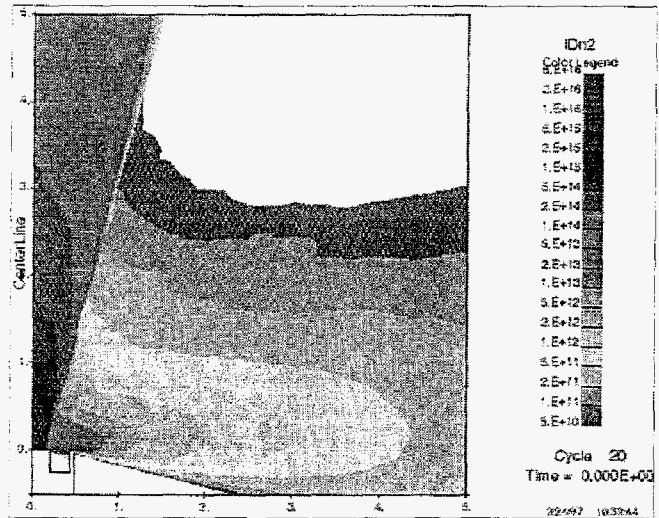


Figure 4. Computed ion density contours for NSTAR ion engine at full power (dimensional scale is meters)

The equality of electron and ion current to the thruster-mask ring determines the relationship of the chassis potential (ϕ) to the plasma-electron temperature (θ):

$$I_e = en \sqrt{\frac{e\theta}{2\pi m_e}} \exp(\phi/\theta) = I_i = en_i \sqrt{\frac{e\theta}{2\pi m_i}} (1 - \phi/\theta) \quad (3)$$

Rearranging and simplifying gives:

$$\exp(\phi/\theta) = \sqrt{\frac{m_e}{m_i}} (1 - \phi/\theta) \quad (4)$$

This equation is solved numerically for ϕ/θ and is satisfied with a value of -4.5. Chassis potential is related to the plasma potential (ϕ) by:

$$\phi = -4.5\theta + \phi \quad (5)$$

PIC computations performed prior to flight (Figure 5) predict that the plasma potential (ϕ) near the thruster mask ring is approximately 1.25 V and the electron temperature confirmed by measurement, $\theta = 1.8$ eV. As a result, the chassis potential for DS1 during NSTAR operations is estimated at -6.75 V.

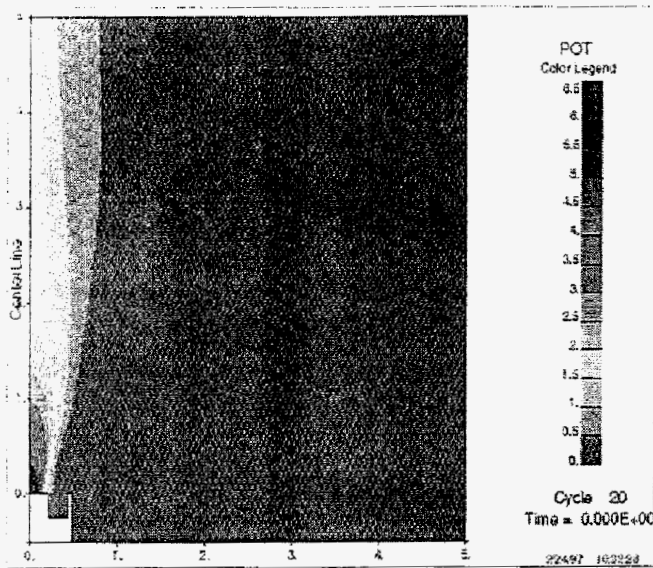


Figure 5. Self-consistent potential computed for NSTAR thruster operating at full power (dimension scale in meters)

As a consistency check for the estimated chassis potential, the variation of the in-flight measured voltage of the IPS internal ground (neutralizer common) with the Langmuir probe bias is compared to ion energies measured by the IDS RPA. During the second IPS performance acceptance test in flight (IAT2) conducted on May 28, 1999, the IDS Langmuir probe sensors were held at four voltage levels (-7 V, -1 V, +5 V, and +11 V, with respect to chassis ground) for a few minutes at each IPS thrust level. The effect on the IPS internal ground is shown in Figure 6.

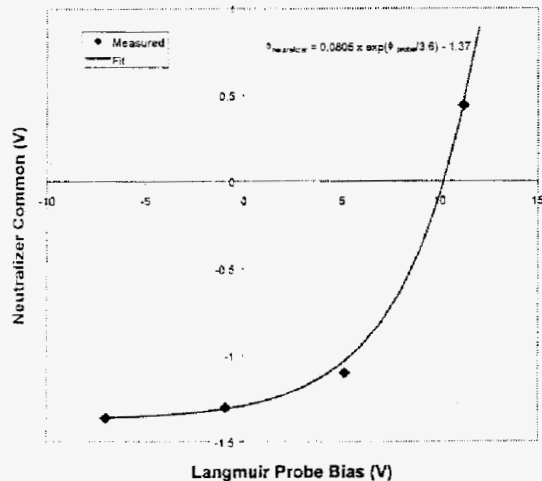


Figure 6. Variation of IPS neutralizer common with IDS Langmuir Probe bias voltage in IAT2

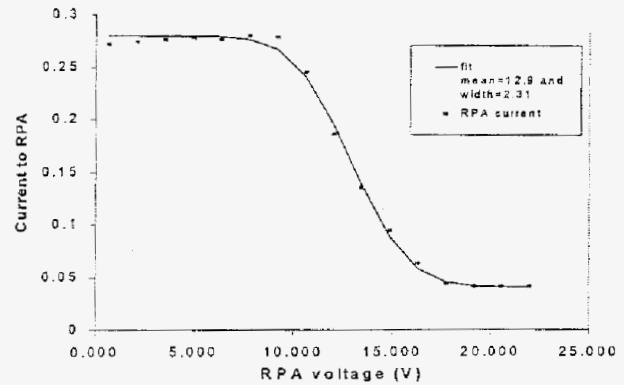


Figure 7a. RPA Sweep at -7-V Langmuir Probe Bias

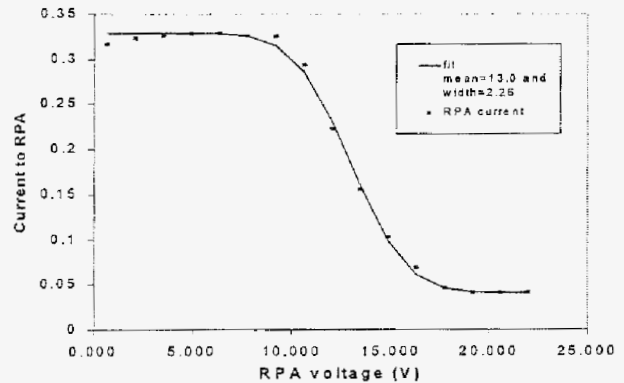


Figure 7b. RPA Sweep at -1-V Langmuir Probe Bias

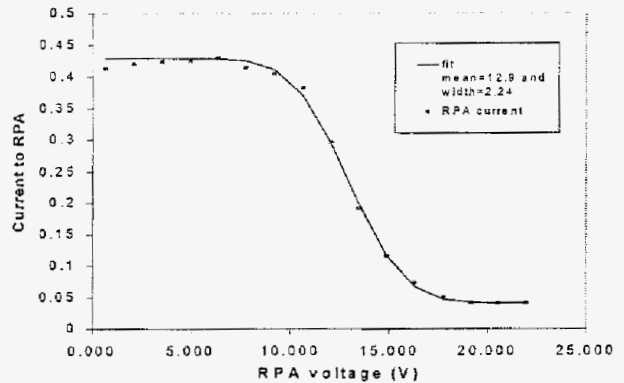


Figure 7c. RPA Sweep at +5-V Langmuir Probe Bias

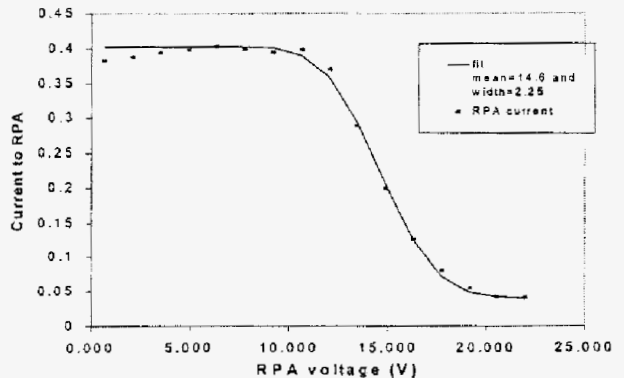


Figure 7d. RPA Sweep at +11-V Langmuir Probe Bias

RPA sweeps obtained at each Langmuir probe voltage level are shown in Figures 7a through 7d. Note the increasing mean ion energy with increasing Langmuir probe bias. The important results from Figures 6 and 7 are summarized in Table 1.

Note that when the Langmuir probe bias is at +11 V, the neutralizer common is 1.75 V higher than when the Langmuir probe bias is near ground. This implies that the DS1 chassis ground is driven -1.75 V due to electron collection by the Langmuir probe at +11 V. During IPS operations, the Langmuir probe is able to drive the DS1 chassis potential from -6.75 V (no bias) to -8.50 V (bias = +11 V).

Table 1. Effect of Langmuir Probe Bias on Ion Energy and Neutralizer Common

Langmuir Probe Bias (V)	Ion Energy (eV)	IPS Neutralizer Common (V)
-7	12.9	-1.35
-1	13.0	-1.3
+5	12.9	-1.1
+11	14.6	+0.45

The estimated net current collection at the thruster mask ring with the Langmuir probe bias at +11 V is 2.75 mA (assuming $\phi/\theta = 5.5$):

$$I_i = Aen\sqrt{\frac{e\theta}{2\pi m_i}}(1 + \phi/\theta) = 4.0 \text{ mA} \quad (6)$$

$$I_e = Aen\sqrt{\frac{e\theta}{2\pi m_e}}\exp(-\phi/\theta) = -1.25 \text{ mA} \quad (7)$$

The measured Langmuir probe current is about 2 mA when biased at +11 V; this is in fairly good agreement with the above-calculated net ion collection at the thruster mask ring.

The voltage of the Langmuir probe with respect to the local plasma potential as a function of Langmuir probe bias is shown in Figure 8. Note that the Langmuir probe will not collect substantial electron current from the plasma until the probe bias has reached approximately +7.5 V.

RPA Current as a Function of IPS Mission Level

Charge-exchange ion production is expected to depend upon IPS operating conditions, since charge-exchange ions are formed by the interaction of beam ions and neutral xenon escaping from the IPS discharge chamber. The expected charge-exchange ion current at the IDS RPA has been calculated for the NSTAR ion engine operating conditions reported in "Engine Table Q." The calculations use velocity-dependent resonant charge-exchange cross

sections computed from the formula provided by Sakabe and Izawa[19]. A transmission factor of 0.27 for the four-grid RPA is based on an individual grid transparency of 0.72. The results of the calculation, with measured RPA currents from IAT2, are illustrated in Figure 9.

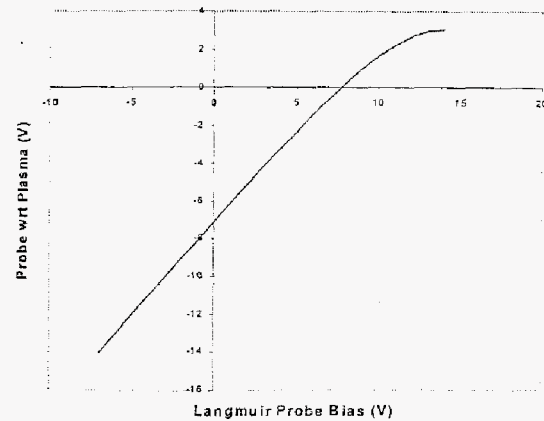


Figure 8. Estimated Langmuir Probe potential versus probe bias voltage

A curious feature in the data shown in Figure 9 is the larger ion current observed at IPS mission level 6 than at higher mission levels (up to 34). In fact, the RPA ion current is 40% higher for mission level 6 than mission level 13. The reason for the enhanced charge-exchange ion production at mission level 6 is the higher relative xenon flow rate in the discharge chamber than the conditions for mission level 13. The excess or residual xenon escaping from the discharge chamber accounts for the higher charge-exchange ion production. Table 2 compares the operating conditions for mission levels 6 and 13.

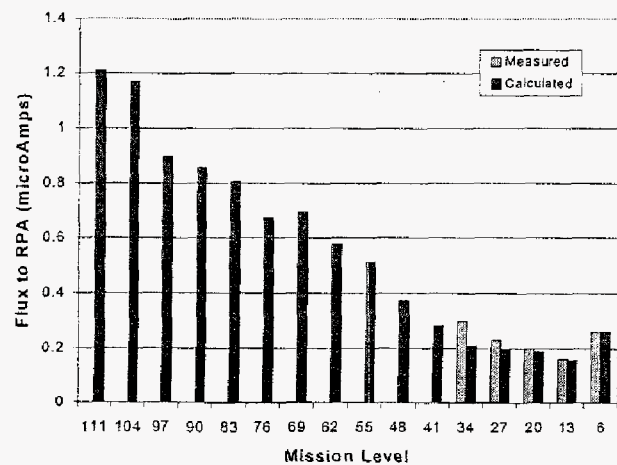


Figure 9. Computed RPA ion current as a function of IPS mission levels (measured currents from IAT2 also shown)

Table 2. Relevant IPS Operating Conditions for Mission Levels 6 and 13

Quantity (units)	ML6	ML13
Total chamber flow (sccm)	8.450	8.290
Total chamber flow (Amps equiv.)	0.606	0.594
Beam current (Amps)	0.509	0.529
Residual Xe flow (Amps equiv.)	0.097	0.065
Beam* residual Xe (Amps ²)	0.049	0.035

The ratio of the product of the beam current and residual Xe for mission level 6 versus 13 is 1.4. This ratio is in good agreement with the measured charge-exchange current ratios for mission levels 6 and 13.

Variation of RPA Current with Ring Langmuir Probe Bias

The placement of the Langmuir probe at the entrance to the RPA causes the probe bias voltage to effect the path of ions approaching the RPA. Figure 10 shows the variation of RPA current with Langmuir probe bias.

The variation in the ion current is attributed to a focusing effect due to Langmuir probe bias. The potential contour and trajectories for ions approaching the RPA with surrounding Langmuir probe at +11 V were computed (see Figure 11). The potential is expressed in terms of the local plasma potential; hence, the entrance to the RPA (chassis ground) is approximately -9.5 V and the ring Langmuir probe bias is +2.5 V. The plasma conditions for this calculation assumes a density of 10^{12} m^{-3} and a temperature of 1.8 eV. The trajectories for 5 eV xenon ions are shown to illustrate the focusing effect of the Langmuir probe.

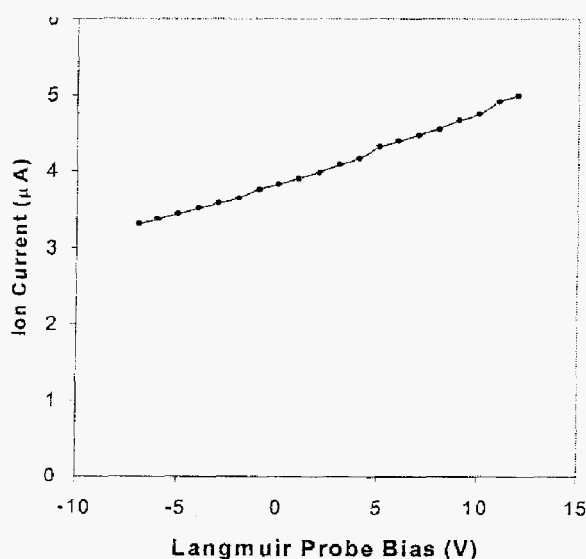


Figure 10. Effect of Langmuir Probe Bias on RPA Current

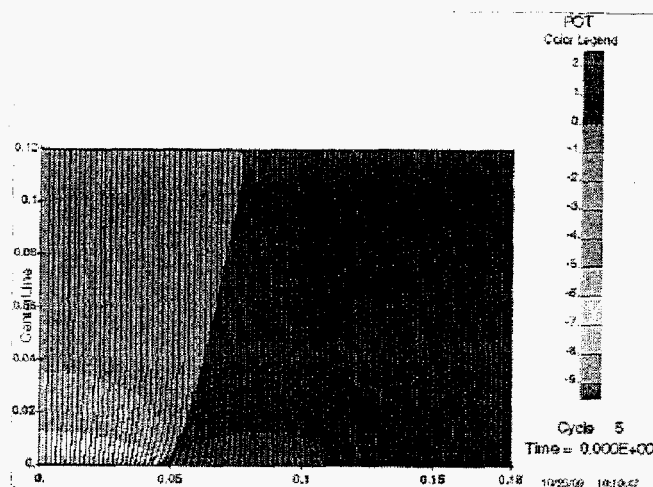


Figure 11. Ion focusing by ring Langmuir Probe at the RPA

Expansion of Langmuir Probe Potential onto Black Kapton

The RPA Langmuir probe is in direct contact with the RSU thermal blanket. The outer layer of this thermal blanket is fabricated from conductive, carbon-filled Kapton film. This black Kapton material provides a resistive path from the Langmuir probe to the spacecraft chassis (ground). The effect of the blanket surface on effective probe size was calculated. The expansion of the probe bias onto the blanket surface is shown in Figure 12. The conductive blanket effectively doubles the size of the RPA Langmuir probe.

Over course of the mission, the effective resistance from the RPA Langmuir probe to the spacecraft chassis decreased due to deposition of molybdenum sputtered from the ion engine grid. At the time of IAT2, the effective resistivity of the film was 17 kΩ per square. The resistive component to the Langmuir probe current is easily removed to allow temperature determination as shown in Figure 13.

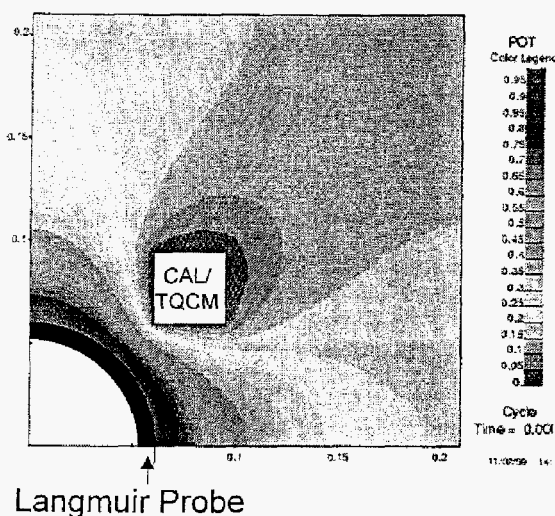


Figure 12. Expansion of Langmuir Probe bias onto RSU thermal blanket

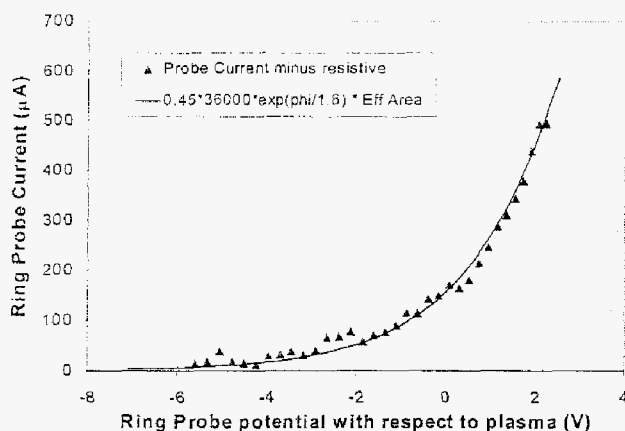


Figure 13. Langmuir Probe least squares fit ($\theta = 1.8$ eV)

Expansion of Charge-Exchange Plasma Around DS1

This subsection describes results obtained by computer modeling of the expanding charge-exchange ion cloud around the DS1 spacecraft¹¹. The charge-exchange plasma produced near the IPS thruster exit was easily detected by the PEPE instrument, located at the opposite end of the DS1 spacecraft. A particle-in-cell (PIC) computer model was constructed to simulate the charge-exchange ion plasma environment surrounding the DS1 spacecraft, especially in the backflow region (upstream of the thruster plume). The physics of the charge-exchange plasma back-flow is similar to that of plasma expanding into a vacuum or wake. The expansion fan is a pre-sheath for the spacecraft, which turns the trajectories of the ions into the upstream direction until they enter the sheath of the spacecraft.

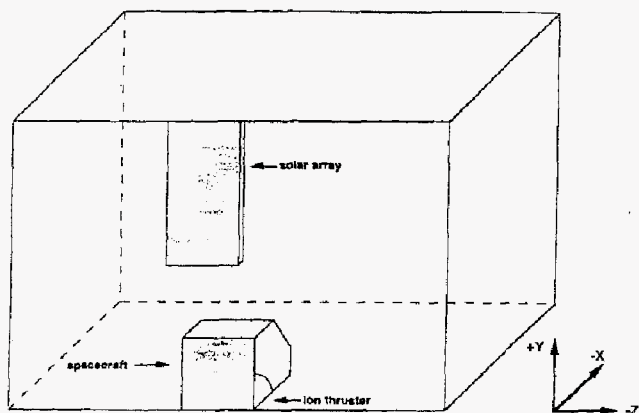


Figure 14. Model geometry for PIC simulation

The model is a full three-dimensional PIC simulation in which the DS1 spacecraft and solar-array elements are included, as shown in Figure 14. For efficiency in computation, the $43 \times 43 \times 71$ grid cells used were uniform in size ($d \approx 6$ cm). Approximately 5 million particles were simulated in steady-state conditions.

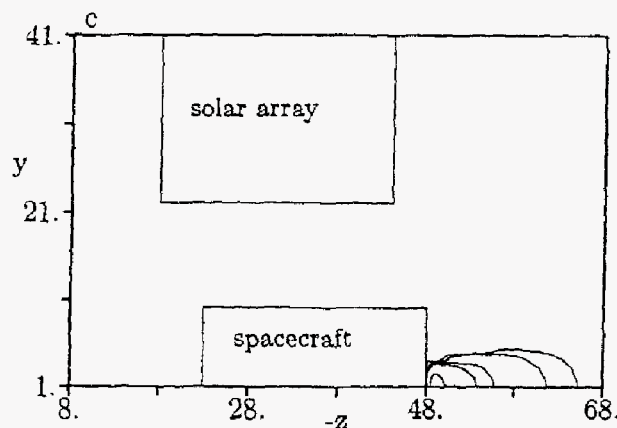
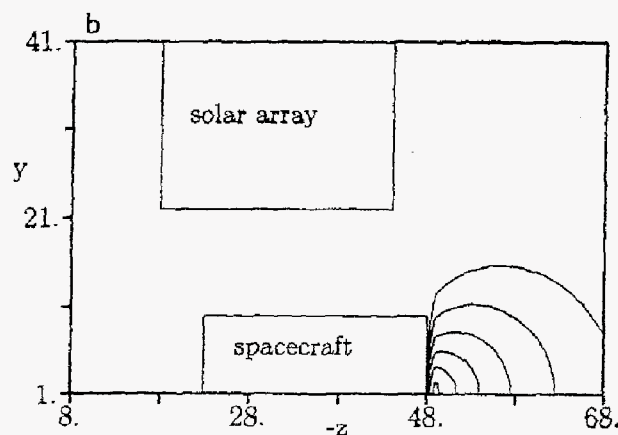
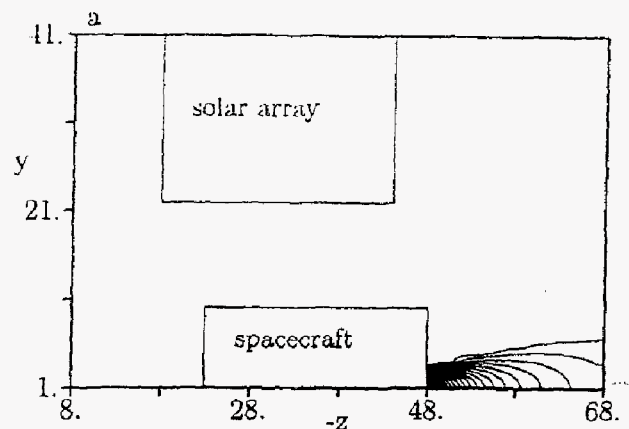


Figure 15. Contour plots for: (a) Beam ion density, (b) Neutral xenon density, and (c) Charge-exchange ion production rates

The electrons were included as a fluid with a Boltzmann distribution based on the electron temperature measured by the IDS (approximately 2 eV). Inputs to the simulation include the beam ion density, neutral density, and charge-exchange ion-production rate near the thruster exit. Figure 15 illustrates the beam-ion density, neutral-xenon density,

and charge-exchange production rate downstream of the DS1 ion engine. The beam and neutral-density plot contours are normalized to the peak densities at the engine exit plane at uniform intervals of 0.05. The charge-exchange ion production rate is also normalized to the peak rate at the engine exit; however, the contours are given on intervals of 0.005, 0.01, 0.05, 0.1, 0.5, and 1.0.

The results of the PIC simulation are illustrated in Figure 16. Figure 16 provides plots of (a) the plasma-electric potential, (b) normalized electric-field vectors, (c) charge-exchange density and (d) charge-exchange ion-flow field vectors around the DS1 spacecraft.

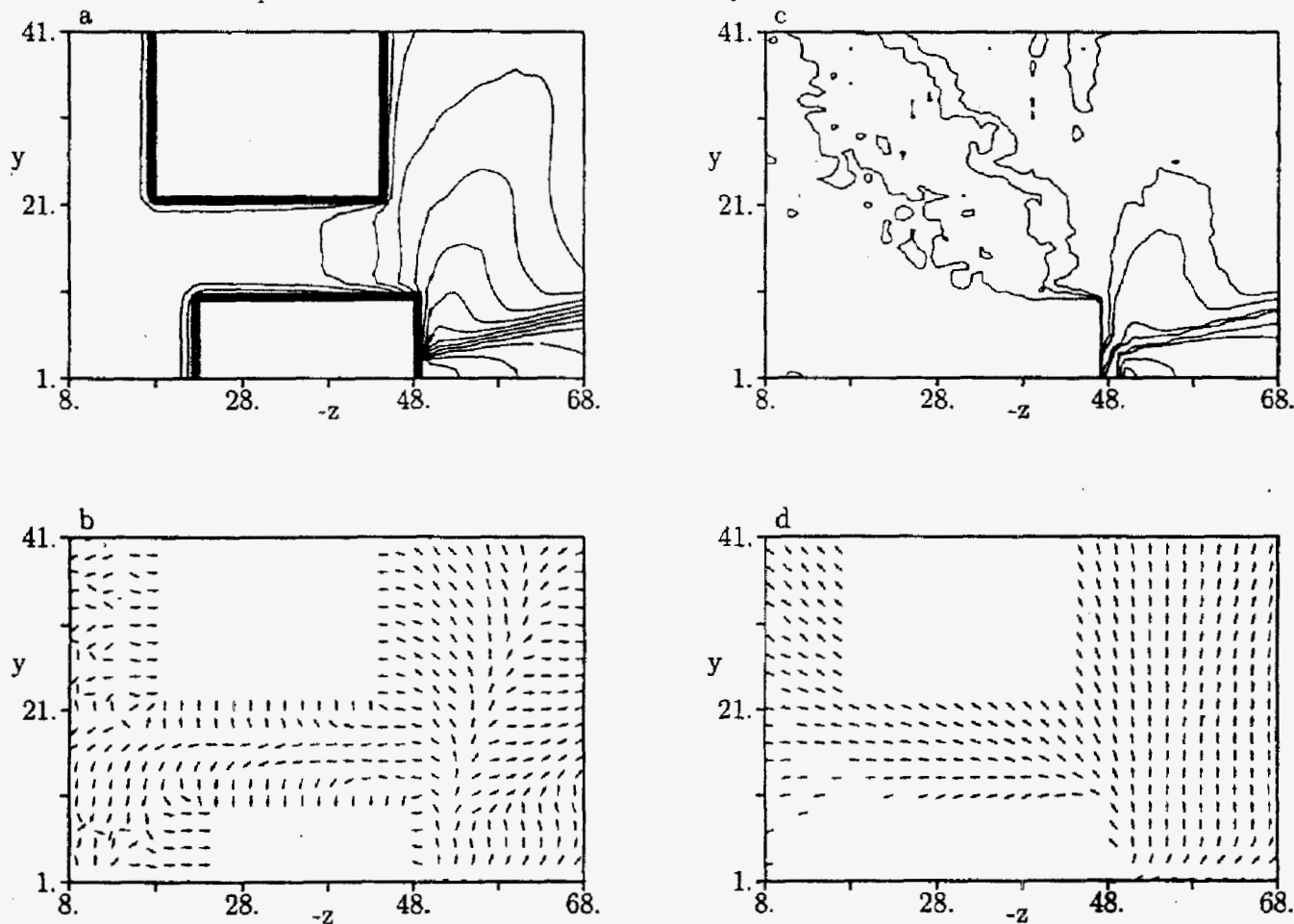


Figure 16. Results of the DS1 PIC simulation: (a) Electric field potential, (b) Electric field direction, (c) Charge-exchange ion densities, and (d) Charge-exchange ion flow directions

The peak potential is 19 V with respect to spacecraft ground and is shown in Figure 16a at 1-V intervals. The direction of the electric-field gradients, illustrated in Figure 16b, clearly shows how the charge-exchange ions are accelerated into the backflow region. The PIC simulation estimates the charge-exchange ion density to be approximately 10^6 cm^{-3} near the IDS, decreasing to 10^4 cm^{-3} near PEPE. Figure 16c shows the charge-exchange ion density distribution around DS1 and the direction of flow of the charge-exchange ions. The charge-exchange density near DS1 during IPS operations is at least three orders of magnitude greater than the ambient solar-wind plasma density.

CONTAMINATION ASSESSMENT

The NSTAR Diagnostics Element has produced useful data regarding the IPS contamination environment. The 8000-hour Life Demonstration Test (LDT) afforded the opportunity to measure the thickness and composition of deposits accumulated at various angles from the ion engine after extended operation. The IDS flight-contamination monitors were positioned to monitor direct, line-of-sight deposits as well as non-line-of-sight contamination from the NSTAR ion engine grid (see Figure 17). The IDS flight contamination monitors functioned properly and provided high-quality data regarding deposition rates as a function on IPS thrust level.

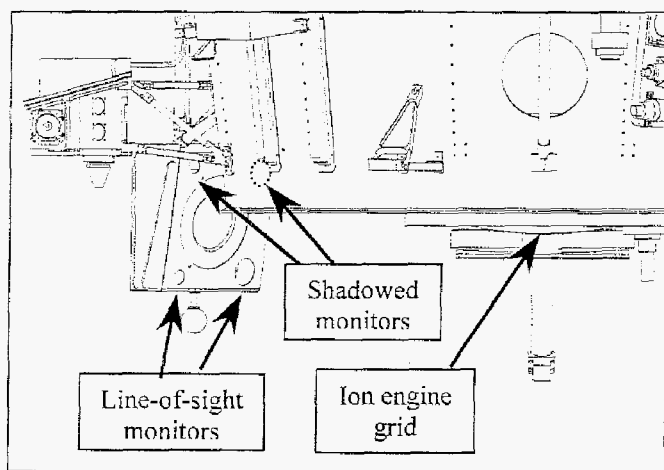


Figure 17. Configuration of IDS contamination monitors on DS1.

Ground Test Contamination Results

The NSTAR 8000-hour LDT was performed at JPL to validate the long life of the NSTAR thruster. A fundamental purpose of the LDT was to assess the effects of extended operation on the engine, especially the grids and cathodes. The grid wear-out mechanism is loss-of-grid material (molybdenum) via sputtering by charge-exchange xenon ions⁹. A significant portion of the sputtered grid material is emitted outward from the engine. In the ground-test environment, chamber effects can strongly effect the results for contamination-witness specimens. The LDT chamber walls were lined with graphite plates to reduce the amount of material sputtered back onto the engine¹⁰. The contamination monitors described below were designed to minimize sputtered material from the chamber walls.

LDT Contamination Monitors—A series of collimated 1-inch diameter fused-silica windows were mounted on a curved support beam 46 inches (1.2 m) from the engine (see Figure 18). The witness monitors were placed at angles from 40° to 110° from the thrust axis, at 10° intervals. To avoid collection of sputtered chamber material, the witness

windows were placed in long (25 cm) tubes lined with tantalum foil. At the entrance of the tube, a collimating aperture was positioned to limit the witness field-of-view to the ion-engine grid. Shadow wires (tungsten) were positioned on the windows to facilitate profilometry measurements.

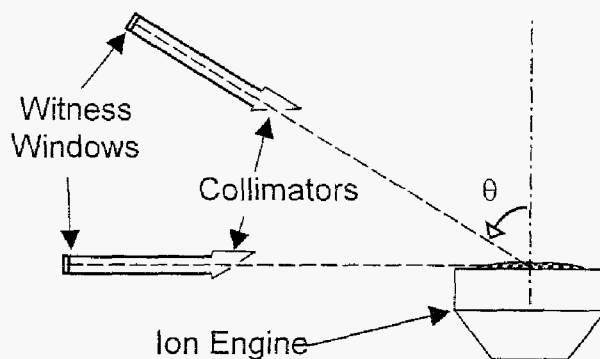


Figure 18. Geometry of collimated contamination monitors for the NSTAR LDT (drawing is not to scale).

Subsequent to the completion of the 8000-hour LDT, the contamination witnesses were removed from the collimation tubes for analyses. Visual inspection of the windows clearly showed a metallic film for witnesses located between 60° and 110° from the thruster beam axis. The metal films appeared hazy or crazed, not highly specular as a uniform flat coating would appear. Attempts to measure film thickness using a profilometer were not very successful. Examination via a scanning electron microscopy (SEM) revealed that the metallic films were wrinkled, presumably due to stresses in the coating and poor adhesion to the substrate. In the regions where the profilometer stylus had contacted the film, the film was scraped from the substrate surface. It was possible to determine the thickness of the coatings in these disturbed areas with SEM imaging. Figure 19 shows LDT deposition at 10° increments between 60° and 110° from thrust axis. The uncertainty in the thickness measurements is on the order of 10%. Currently, there is no firm explanation for the apparent enhanced deposition observed at the 80° position. It is likely that erosion from the edges of grid holes could lead to a complex angular deposition distribution²⁰. X-ray dispersive spectroscopy (XDS) of the metal films revealed their composition to be molybdenum metal (no evidence of tantalum contamination), with a significant amount of xenon detected. The source of the xenon is either from background xenon within the LDT vacuum chamber or, possibly, impingement of low-energy (<10 eV) charge-exchange xenon ions. The witness monitors at 50° and 40° were found to be eroded 1.7 and 7.7 μm. Energetic xenon ion sputtering causes the erosion of these witness monitors. The witness monitors at larger angles may also be impinged by xenon ions capable of sputtering material, but not at a sufficient flux to prevent deposition of sputtered molybdenum.

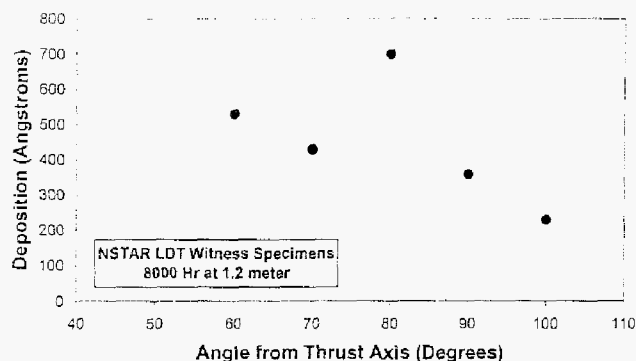


Figure 19. Molybdenum accumulation for NSTAR LDT witness monitors versus angle from thruster axis

Flight Correlation—On DS1, the line-of-sight contamination monitors are located 75 cm from the thruster centerline, 85° off thrust axis. Even though the grid is an extended source, the deposition thickness is roughly inversely proportional to square of distance from grids. A contamination witness located at the DS1 QCM0 position would have accumulated approximately 1300 Å during LDT. Rates of contamination accumulation during IPS thrusting can be conveniently expressed in terms of Angstroms of molybdenum per 1000 hour (1 khr) of operation. The expected deposition rate for an LDT witness monitor in the equivalent position of the line-of-sight IDS contamination monitor is 160 Å/khr.

Flight Contamination Results

The quartz crystal microbalance (QCM) sensors mounted in the IDS Remote Sensors Unit have produced useful data for assessing the contamination environments on DS1. The IDS QCM sensors are 10-MHz fundamental-frequency devices; hence, the frequency-to-area-mass-density conversion is $4.43 \text{ ng/cm}^2\text{-Hz}^{16}$. QCM beat frequencies are sensitive to changes in temperature and solar illumination of the sense crystal. To extract low-level contamination information, QCM data often must be corrected for temperature and solar illumination. The magnitude of the IPS-induced contamination for the line-of-sight (QCM0) sensor is such that these corrections are not necessary. The non-line-of-sight (QCM1) sensor, though, had significantly less accumulation; therefore, its data should be corrected prior to precise quantitative interpretation. The data, as presented in this paper, have not been corrected for sense crystal temperature or solar illumination. The results are discussed chronologically in this section.

Launch Operations—The final pre-flight functional test of the IDS prior to launch was conducted on DOY 293-1998. Data from the QCMs provide the pre-launch baseline for assessing launch-phase contamination in the vicinity of the DS1 to launch-vehicle interface. The pre-launch

readings were obtained at 16 °C and are 2475 Hz and 2085 Hz for QCM0 and QCM1, respectively. Following launch, DS1 was oriented with the Sun vector aligned with the spacecraft X-axis. In this orientation, QCM0 is illuminated with a Sun angle of approximately 46°, whereas QCM1 is in the shadow of the DS1 propulsion module. The IDS was not activated until 1998-298 at 2201 hour (approximately 34 hours after launch). The initialization of IDS included a special activity ("DFrost") intended to bake-off volatile contamination from the QCMs and calorimeters by heating the sensors to +75 °C. Very little change (<50 Hz) was observed in the beat frequency of either QCM as a result of the initial post-launch DFrost.

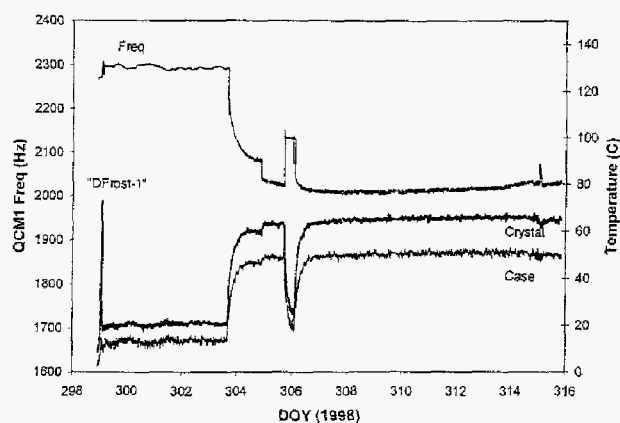


Figure 20. QCM1 (non-line-of-sight) early mission response.

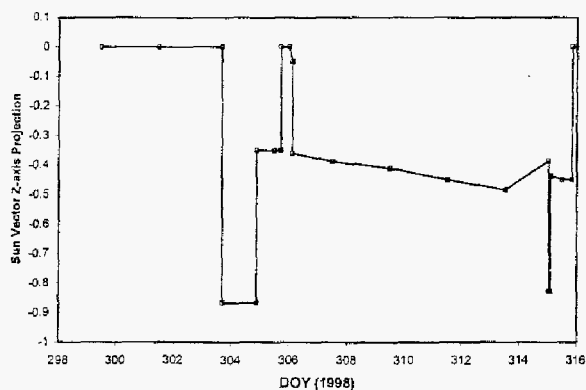


Figure 21. Early mission DS1 Sun orientation

The frequencies and temperatures for QCM0 and QCM1 just prior to DFrost were 2260 Hz (at +30 °C) and 2272 Hz (at +16 °C) respectively. Since QCM0 was exposed to the sun after launch, it is suspected that most of the contaminants accumulated on it were evaporated prior to IDS initialization. The beat frequency for QCM1 increased by 187 Hz from pre-launch to IDS initialization, yielding an estimated $0.8 \text{ } \mu\text{g/cm}^2$ (80 Å) accumulation for launch-phase contamination. This accumulation was not affected by the DFrost activity, but was removed when DS1 rotated to expose the NSTAR ion engine to the Sun (NSTAR

Decontamination Maneuver). Figure 20 shows the early mission response of QCM1 to the DS1 orientation with respect to the Sun shown in Figure 21. Note the substantial frequency and temperature changes near DOY 304-1998 associated with the NSTAR Decontamination Maneuver. There is an additional turn on DOY 305-1998 that further effects the QCM1 frequency and temperature. On DOY 306-1998, DS1 returned to the nominal Sun on X-axis orientation. Using the frequency reading at this time, it appears that about a 165-Hz decrease occurred as a result of this solar-stimulated bakeout. Based on this interpretation of QCM1 data, it appears that the RSU surfaces were contaminated during the DS1 launch phase with approximately 80 Å of low-volatility organic material, most of which was removed upon exposure to the Sun.

IPS Operations.—The QCM data for the IPS operations for DS1 are illustrated in Figures 22a and 22b. Higher resolution plots of the QCM data for the first year are presented in Appendix A, Figures A1a through A1h.

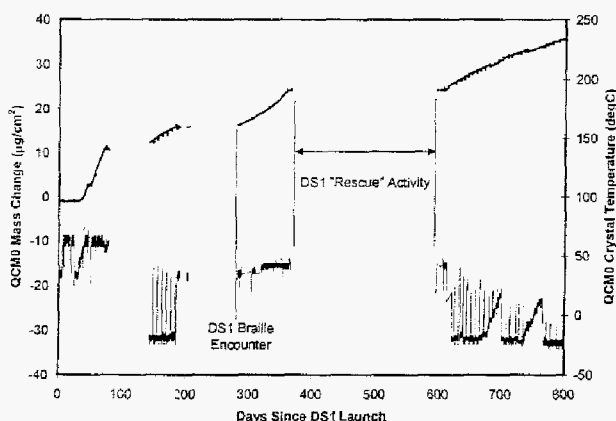


Figure 22a. Mass accumulation on the line-of-sight QCM on DS1. Data is plotted only for IPS thrusting periods.

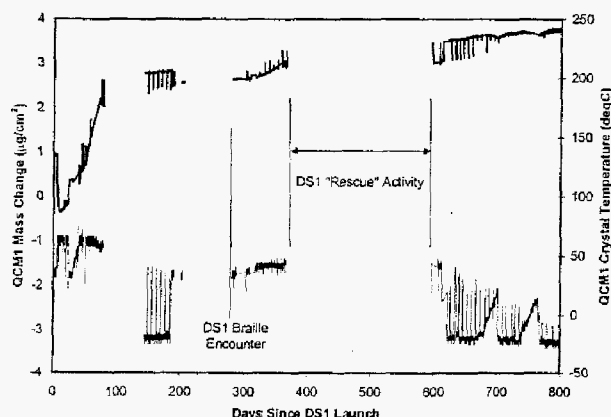


Figure 22b. Mass accumulation on the non-line-of-sight QCM on DS1. Note that mass scale is expanded by x10.

The figures are arranged so the response of the line-of-sight (QCM0) and non-line-of-sight (QCM1) sensors can be readily compared. The data segments in the figures represent time intervals during which IPS operations of substantial duration occurred. Data for minor thrusting events, such as the brief "S-Peak" test on DOY 022-199 and the trajectory correction maneuvers prior to the Asteroid Braille encounter, do not show significant accumulations on either QCM. Similarly, data for the long, non-thrusting intervals are not shown because no accumulation occurred on either QCM in these periods. No data was collected during the "DS1 Rescue" activity since IDS was inactive while the mission operations team developed the control software to utilize the science camera in place of the failed star tracker.

Since launch, the line-of-sight sensor (QCM0) has collected 35 µg/cm² of mass, which corresponds to a 340 Å thick molybdenum film. The shadowed sensor (QCM1) has collected 3.5 µg/cm² of mass, which corresponds to a 34 Å thick molybdenum film. For the thrusting conditions thus far, the shadowed QCM has accumulated approximately 10% of molybdenum deposited on the line-of-sight sensor. Pre-flight estimates anticipated an order of magnitude less accumulation on the shadowed QCM1 than what has been measured. It is possible that a small portion of the deposited mass on the shadowed QCM is not molybdenum, perhaps from general spacecraft outgassing contamination. The primary source of the non-line-of-sight accumulation is attributed to ionized molybdenum, moving along trajectories effected by electrostatic potentials associated with the thruster plume and spacecraft surfaces. The pre-flight estimates were based on electron impact ionization of neutral molybdenum atoms sputtered from the grid. The possibility of charge-exchange between xenon beam ions and sputtered molybdenum atoms is under consideration. Since the DS1 solar arrays do not extend into the line-of-sight zone, are well removed from the thruster (>2 m), and are negatively grounded, the amount of molybdenum deposited on the SCARLET concentrator lenses is expected to be very small.

Deposition Dependence on IPS Mission Level.—The deposition rates for QCM0 and QCM1 at various NSTAR mission levels are summarized in Figure 23. The effective deposition rate for the full power LDT is indicated in the right-hand side of the figure. Due to the IPS operations profile, there is no data available for mission levels 50 through 70. As indicated before, the line-of-sight QCM0 accumulates molybdenum at a substantially higher rate than the shadowed QCM1. The line-of-sight sensor deposition rate appears roughly proportional to the square of the mission level, whereas the non-line-of-sight rate seems more strongly affected by mission level. The rate of production of ionized molybdenum is expected to increase dramatically with mission level for the following reasons²¹:

- More sputtered molybdenum atoms are produced at higher mission levels due to increased impingement by charge-exchange xenon.
- Higher electron temperatures are observed at higher mission levels, increasing the rate for electron-impact ionization of neutral molybdenum.
- More beam ions are produced by the engine, increasing the rate for possible charge-exchange ionization of molybdenum atoms.

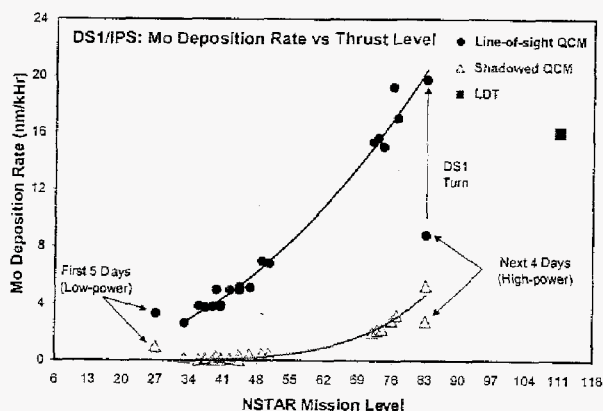


Figure 23. Mo deposition rates versus mission level (QCM0 is the line-of-sight sensor)

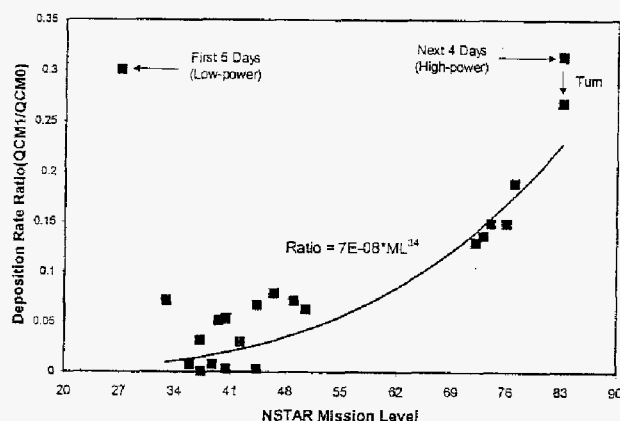


Figure 24. Ratio of non-line-of-sight to line-of-sight deposition rates as a function of mission level

The molybdenum collection rate by the non-line-of-sight sensor normalized to that of the line-of-sight QCM is shown in Figure 24. The ratio appears to increase strongly with mission level. The early mission data points highlighted on the plot correspond to initial IPS operations at low and high mission levels that show an enhanced collection rate by the non-line-of-sight sensor. It is possible that this enhancement is due to contamination from spacecraft outgassing, since the ion engine heats the propulsion module assembly during operation. It is also possible that spacecraft outgassing contributed to the trend at high mission levels (> 70), since the early mission profile consisted of gradually decreasing

thrust. Unfortunately, this ambiguity may not be directly resolved in the future because the Sun distance for DS1 will remain above 1.3 AU for the remainder of the mission, precluding IPS operations at mission levels greater than 50. Correlation of these rates with certain IPS telemetry, such as the accelerator grid impingement current, have thus far failed to improve the understanding of the mission-level dependence.

Thermo-optical Property Changes—The IDS contamination monitors include line-of-sight and non-line-of-sight calorimeters. Under ideal conditions for analysis, calorimeters should have a 2π -steradian field-of-view to space. Of course, this condition is clearly not possible for the line-of-sight calorimeter. The requirement for Sun-viewing and the desire to correlate mass deposition with thermo-optical property changes drove the configuration of the non-line-of-sight calorimeter to the present state. The presence of the DS1 spacecraft (with IPS thruster) in the field-of-view of the calorimeters has substantially complicated the data analysis for these sensors. Some semi-quantitative analysis is possible for the line-of-sight calorimeter. The temperature of this calorimeter increased dramatically in the early part of the mission, as seen in Figure 24.

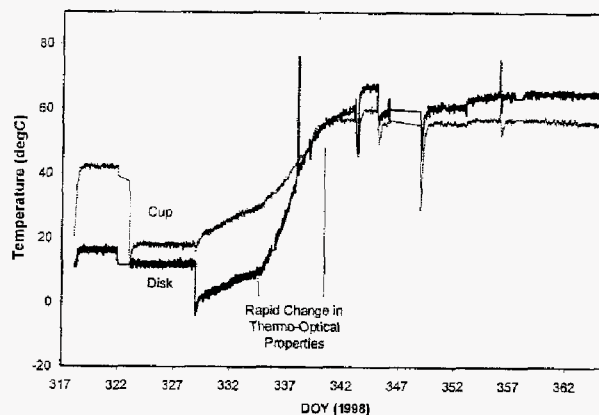


Figure 25. Response of IDS line-of-sight calorimeter during initial IPS operations

The active calorimeter element (the disk) increases in temperature by more than 50°C within several days of high mission-level operation of the IPS thruster. The solar illumination of the calorimeter, illustrated in Figure 26, remained constant at about 93 mW/cm^2 from DOY 323-1998 through 338-1998. DS1 turned to the trajectory thrust attitude on DOY 338-1998, reducing the solar input to approximately 75 mW/cm^2 . The solar input gradually decreased to 70 mW/cm^2 until DOY 343-1998, when DS1 again changed attitude. The relatively constant period of solar illumination between DOY 322-1998 to 339-1998 provides the opportunity to simply estimate changes in the thermo-optical properties of the line-of-sight calorimeter.

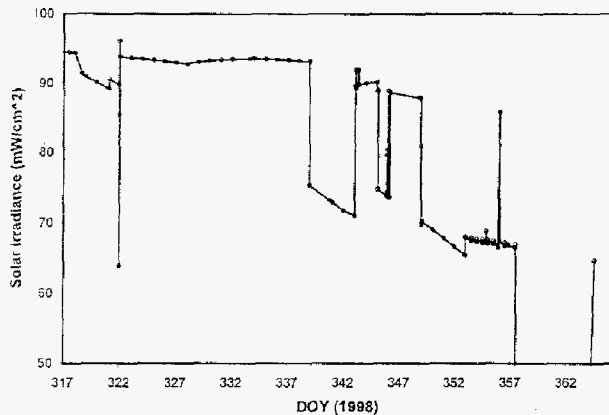


Figure 26. Solar irradiance history for the line-of-sight calorimeter during initial IPS operations

The change in thermo-optical properties for the initial four days of high-power operation is determined from the values in Table 3.

Table 3. Selected Parameters for Estimating the Change in Thermo-optical Properties

Quantity	335-1998	339-1998
Insolation (mW/cm^2)	93.5	93.0
T_{disk} ($^{\circ}\text{C}$)	11.1	45.2
T_{cup} ($^{\circ}\text{C}$)	31.7	48.2
$Q_{\text{disk-cup}}$ (mW)	31	3
T_{sky} (K)	243	243

It is first necessary to estimate the effective sky temperature due to the radiative heat load from the spacecraft and thruster into the calorimeter disk. The initial value for the ratio of solar absorptance to hemispherical emittance (α/ϵ) is taken as the pre-flight value, $0.1 = 0.08/0.8$, since little contamination was encountered during the launch phase. The pre-flight measured conductive heat leak between the disk and cup is $1.5 \times 10^{-3} \text{ W}/\text{cm}^2$. At equilibrium, the radiative heat loss from the disk is equal to the solar-heat input and heat leak from the cup.

$$Q_{\text{rad}} = Q_{\text{sun}} + Q_{\text{disk-cup}} = \epsilon \sigma A (T_{\text{disk}}^4 - T_{\text{sky}}^4) \quad (8)$$

Using the values for DOY 335-1998, effective sky temperature is estimated to be 243 K (-30°C). This value may seem high, but the NSTAR thruster may reach temperatures of 500 K at in operation. The effective sky temperature is assumed to remain constant for DOY 339-1998. Neglecting the minor heat loss between the disk and cup, the estimated value for α/ϵ increases to 0.4. This is a significant change in radiator properties (to typical design end-of-life), with an estimated molybdenum accumulation of about 10 to 15 Å.

IPS PLASMA WAVE & EMI CHARACTERISTICS

Plasma Wave Electric-field Measurements

Ground Test—An IPS compatibility test (ICT) with the DS1 spacecraft was performed in the JPL 25-foot space simulator facility in February 1998. During the ICT, the IPS was briefly operated at TH0 (ML6), TH7-8 (ML55-ML62), and TH14 (ML104) thrust levels. The IDS Engineering Model, which included the flight Plasma Wave Antenna (PWA) pre-amplifier and Plasma Wave Spectrometer (PWS) board from TRW, was used in the ICT. The IDS used a rigid, non-flight 2-m tip-to-tip wire antenna to monitor electric field signals. A flight-like search coil was used to collect AC magnetic field data.

At the time of the DS1 ICT, the IDS software manager was not on-board; therefore, DS1/IDS command and data communications were invoked by primitive commands to the DS1 MIL-STD-1553B bus controller hardware. IDS could not transmit time-domain data in the "burst" mode because no processing of the IDS bus traffic was performed by the DS1 flight computer at this time. Data from IDS were captured by an external MIL-STD-1553B bus monitor. Therefore, the DS1 test conductor only executed IDS configuration or gain commands during periods of low spacecraft activity. No IDS commanding was performed during IPS thrust operations. The IDS team prepared several PWS gain commands in preparation for the ICT. For the initial ML6 operations, the PWS gain was set at a relatively low level. Upon examination of the PWS data, the PWS gain was set to a high level for the remainder of the ICT.

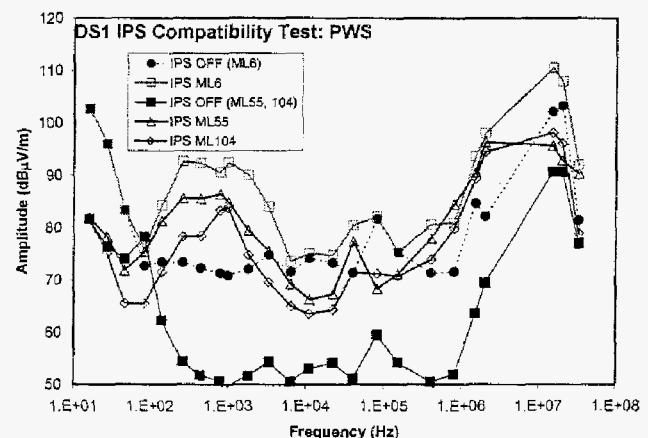


Figure 27. Plasma wave spectra for ICT thrust levels

PWS electric-field data obtained during the DS1 ICT is shown in Figure 27. A few features are readily noted in the power spectra. A large peak appears in the 1-MHz to 15-MHz region, attributed to IPS electron-plasma frequency noise. A lesser peak is seen in the 200-Hz to 4-kHz region;

the source of this signal is not yet understood. The amplitude of the PWS signal is less than $0.1 V_{p-p}/m$, except near 15 MHz, where the signal approaches $0.3 V_{p-p}/m$. Note that there is little signal observed in the 10-kHz to 300-kHz frequency region during the ICT.

Flight Measurements—For purposes of comparison with ground measurements made during the DS1 ICT, data from a brief IPS activity on DS1 to assess power production from the SCARLET solar arrays is presented. This DS1 test, referred to as “S-Peak,” operated the IPS for a relatively brief interval (less than 40 minutes total). The IPS is always started with high-cathode flow rates; the characteristic time to reach steady-state-flow conditions is generally several hours. Therefore, this brief S-Peak test most closely resembles the IPS conditions during the ICT. Due to the spacecraft-to-Sun range, though, DS1 was not able to achieve the ML104 maximum level witnessed in the ICT.

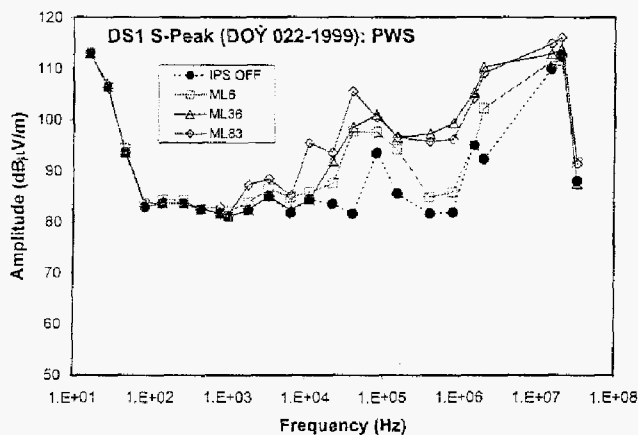


Figure 28. Plasma wave spectra for S-Peak thrust levels

PWS electric-field data obtained during the “S-Peak” test is shown in Figure 28. Since time-domain data collection was enabled to capture high-amplitude events during the S-Peak test, the PWS gain settings were lower than that for the DS1 ICT. The PWS noise “floor” for S-Peak is approximately $0.01 V_{p-p}/m$. The high-frequency feature between 1 MHz and 15 MHz is about 10 dB higher in amplitude in the flight S-Peak than what was observed in the ground-based ICT. Unlike the ICT, essentially no signal amplitude is observed between 200 Hz to 4 kHz during S-Peak. A substantial signal is observed in the 10-kHz to 300-kHz frequency region in the S-Peak data (in contrast to the minimal signal observed in this frequency regime during ICT). Both the ICT and S-Peak data sets appear to show an amplitude “dip” between 300 kHz and 2 MHz.

Characteristic plasma wave signal measurements under IPS steady-state thrust conditions were obtained during IPS Acceptance Tests IAT1 and IAT2. The results for IAT1 are shown in Figure 29. The plot-symbol size approximates the

amplitude-error bars at high signal levels. The PWS signal might be expected to correlate with the thrust level for the IPS. The data in Figure 29 shows no straight-forward correlation between plasma-noise amplitude and IPS-thrust level. Note that the highest thrust level (TH12, ML90) has a plasma-wave spectrum almost the same as that for TH3 (ML27). The highest plasma noise in IAT1 is observed for TH11 (ML83). Maximum signal levels, at 40 kHz, are about $0.2 V_{p-p}/m$ and from 2 MHz to 15 MHz are approximately $0.5 V_{p-p}/m$, similar to amplitudes observed in the S-Peak data. The behavior in the low-frequency region (below 10 kHz) with thrust level is not well understood, but could be due to inter-modulation between switching power-supply modules within the IPS power-processing unit.

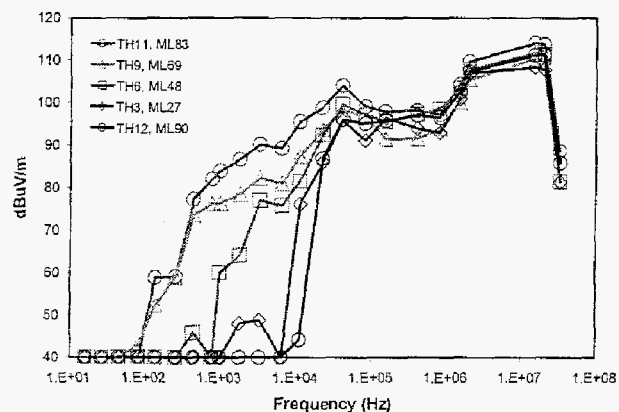


Figure 29. Plasma wave spectra for IAT1 mission levels

Plasma-wave-noise measurements obtained during the lower thrust level IAT2 are shown in Figure 30. Note that the lowest thrust level (TH0, ML6) has a noise spectrum almost as high as that for TH4 (ML34). The spacecraft noise level just prior to initiation of IAT2 is plotted as a solid black line in the Figure. The spacecraft noise includes a signal from an unknown source in the 2-kHz to 7-kHz region. This signal appears to be attenuated by thruster operations at ML13 through ML26. Maximum signal levels, at 40 kHz and 2 MHz to 15 MHz, approach $1V/m$. Again a characteristic “dip” in the spectrum is observed in the 300-kHz to 1-MHz frequency region.

The plasma noise from the IPS occasionally changes dramatically during thrust-level transitions. Upon transition to a higher thrust level, the IPS is designed to first increase the xenon flow, then increase the ion-beam current and other IPS electrical parameters. Increased xenon flow at a fixed beam current, will increase the production of charge-exchange xenon. This charge-exchange xenon plasma behaves as an electrically conducting medium for the plasma noise. A dramatic example of this behavior is illustrated in Figure 31. The amplitude of the plasma noise in the 22-kHz band increases by 100-fold during the 2-minute transition from ML20 to ML27. Note that the

steady-state plasma wave signatures for these two thrust levels are within a factor of two of each other.

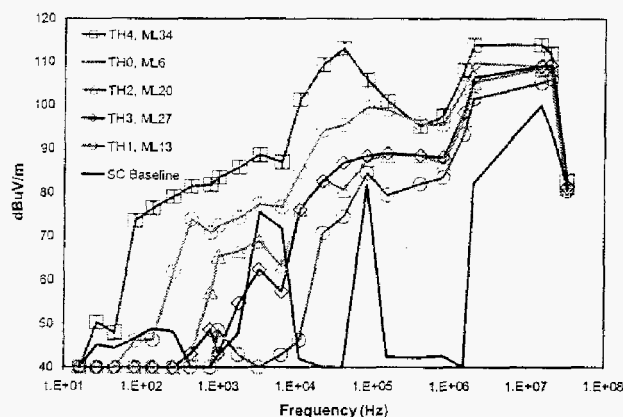


Figure 30. Plasma wave spectra for IAT2 mission levels

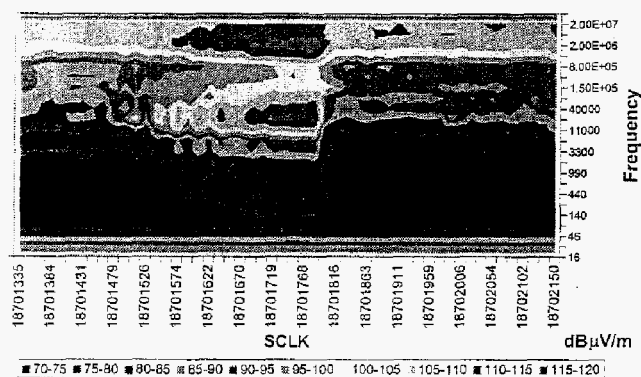


Figure 31. Plasma wave spectrogram for IPS transition from ML20 to ML27

The transition between IPS ML83 to ML90 is shown in Figure 32. In this case, the plasma noise decreases dramatically in the lower frequency region (<10 kHz). This phenomenon has been repeated in ground test by reducing neutralizer flow or discharge current. In the ground test, it is possible for a secondary plasma sheath associated with the chamber walls to envelope a portion of the antenna. In flight, the higher noise level at ML83 might be due to the amount of residual xenon available for producing a noisy plasma discharge within the neutralizer. Further experimentation in flight will not occur until after completion of the extended science mission because reduced xenon flow represents an erosion risk to the cathodes. (A common plenum tank controls both the NSTAR IPS neutralizer and discharge cathodes; therefore, the erosion risk exists for both devices.)

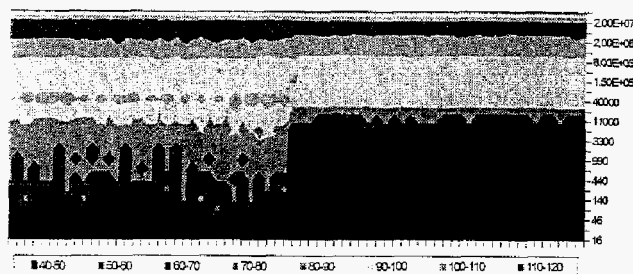


Figure 32. Plasma wave spectrogram for IPS transition from ML83 to ML90

AC Magnetic Fields (EMI)

Ground Test—In addition to the electric-field measurements, the IDS made simultaneous measurements of AC magnetic fields during the DS1 IPS compatibility test (ICT). In spite of setting the gain to the maximum level after the TH0 (ML6) initial firing of the IPS, no signals above the noise floor were recorded during the test. Prior to and subsequent to IDS delivery to the ICT, the IDS engineering model search coil easily detected AC magnetic field stimuli applied with a small excitation coil. The absence of AC magnetic signature in the ICT ground test is very surprising, given the amplitudes observed in flight.

Measurements were made with engineering model search coil in NSTAR characterization tests CT31 and CT36, capturing signals with a fast digital oscilloscope. As seen in Figure 33, the search coil shows a weak response to transient events, such as the IPS engine start, but does not show much electromagnetic interference (EMI) noise with steady-state engine operations. Whether the lack of strong AC magnetic signals is due to chamber effects or EMI-shielding or grounding considerations is under debate.

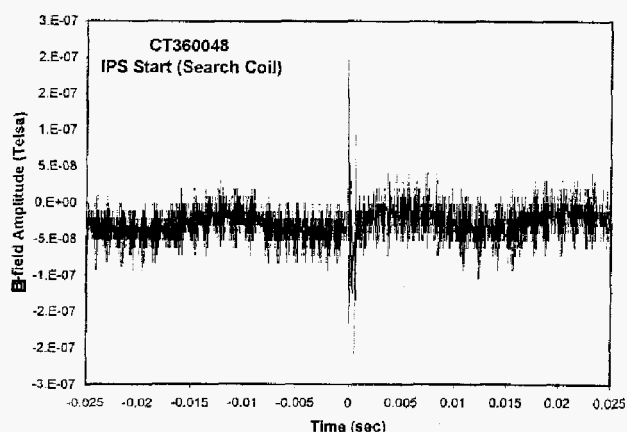


Figure 33. Response of the Search Coil Magnetometer to IPS start during ground testing

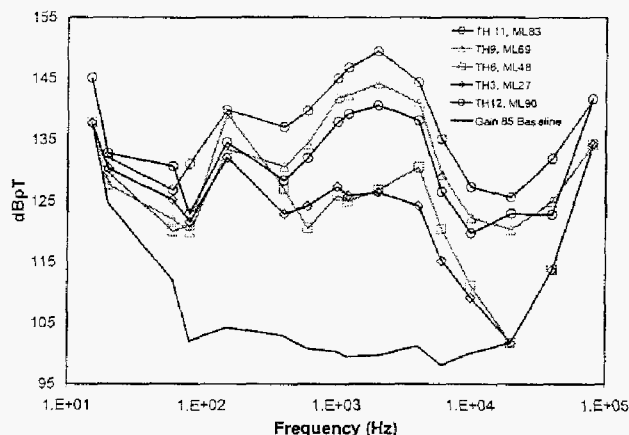


Figure 34. Magnetic field spectra for IAT1 mission levels

Flight Measurements—AC magnetic-field data recorded by the IDS engineering search coil (SCM0) during IAT1 is shown in Figure 33. Some of the characteristic trends observed in the electric-field data (Figure 29) are also seen for the magnetic (B-fields). The highest amplitude B-fields are found at ML83 in the 1-kHz to 5-kHz region. The peak amplitude for ML90 is 10 dB below that of ML83, as found in the E-field spectra. The lowest B-fields in IAT1 are found at ML27 and ML48, which differs from the E-field measurements where ML90 was the least-noisy operating point. The lower-frequency signals (50 Hz to 200 Hz) appear to have less variation with operating level and are not consistent with the order witnessed in the 1-kHz to 5-kHz region. Until the IAT2 test was performed, the nature of the low-frequency magnetic field signals were not understood.

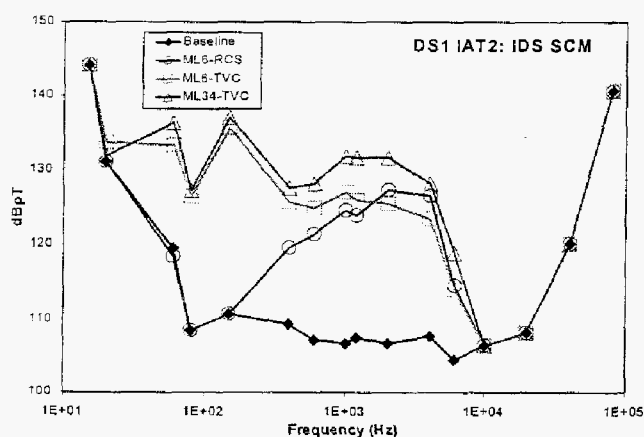


Figure 35. Magnetic field spectra for IAT2 mission levels

Data obtained during the DS1 IAT2 activity is shown in Figure 35. The figure shows the relative contribution to a known non-IPS source of EMI on the DS1 spacecraft: the engine gimbal assembly (EGA) stepper-motors for performing thrust vector control of the IPS engine. IAT2 included special EGA motion patterns for magnetic field

and charge-exchange plume mapping experiments (this data is still under analyses). The attitude control system software maintained DS1 pointing using only the reaction control subsystem (RCS) hydrazine thrusters during this period of IAT2. As a result, the DS1 search coils could distinguish between EMI produced by the EGAs and the IPS during ion engine operations. Note that the EGA noise amplitudes are comparable to IPS noise, though at much lower frequency (< 400 Hz).

Plasma Wave Transient Signals

Ground Test—As indicated earlier, the DS1 flight software to control the IDS was not available during the ICT. Time-domain data from the plasma wave antenna and search coil sensors could not be captured during this integrated ground test of DS1 and IPS. Time-domain waveform data from plasma wave antennas were recorded during NSTAR developmental and characterization tests using flight-like sensors and laboratory digital oscilloscopes.

Examples of a typical high-amplitude, IPS-generated event are shown in Figure 36 and Figure 37. This event occurs during discharge ignition during IPS start-up. An actively amplified monopole antenna detected the data in Figure 36. The amplitude of this event is 8 V_{p-p}/m. Data shown in Figure 37 was simultaneously recorded with a 2-m tip-to-tip dipole antenna with an engineering model IDS PWA pre-amplifier. Notice that amplitude recorded by the dipole antenna is only about 2 V_{p-p}/m, about a factor of 4 less than the monopole signal.

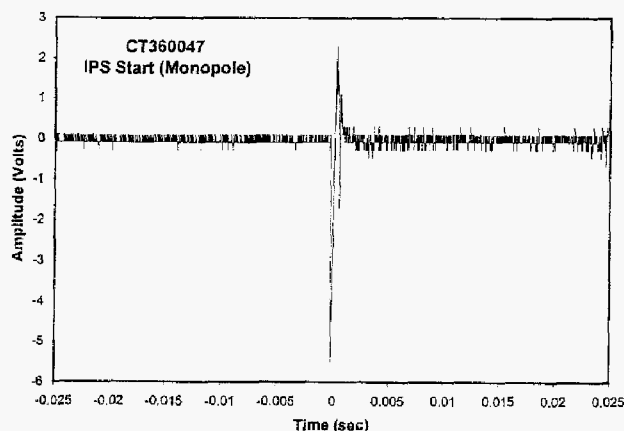


Figure 36. IPS ignition in CT36 ground test (monopole)

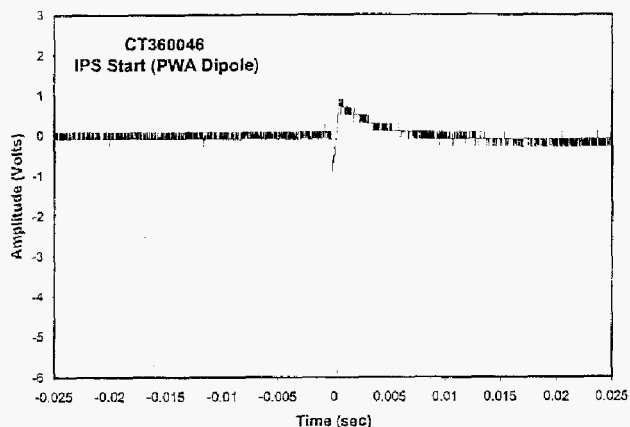


Figure 37. IPS ignition in CT36 ground test (PWA dipole)

The IDS recorded several IPS-ignition events in flight. Data for a typical IPS ignition is shown in Figure 38 below. The peak signal at $t=0$ seconds is approximately 1 V/m, consistent with the level observed in PWA dipole measurement from the CT36 ground test. After the ignition event, the noise from the IPS plasma is clearly visible in the IDS PWA data. Simultaneous magnetic field data for IPS ignition from the IDS search-coil magnetometer is displayed in Figure 39. Peak field strengths of about 50,000 nT are observed for IPS-discharge ignition.

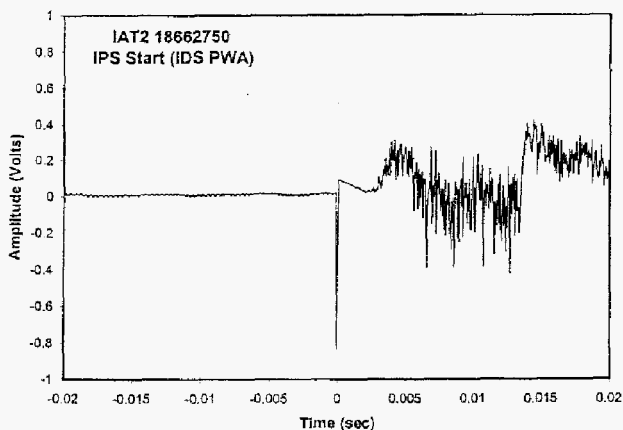


Figure 38. E-field transient signal for flight IPS ignition

The IPS can also produce high-amplitude transient-field events when a momentary ionization arc between the grids induces a "recycle" event. The NSTAR power processor unit will disable the ion beam power supplies within a few microseconds of a fault condition in the output. Within a second of disabling the beam supplies, the power processor gradually restores the beam supplies to the thrust level. Examples of the E- and B-field transients for a recycle event are shown in Figures 39 and 40, respectively.

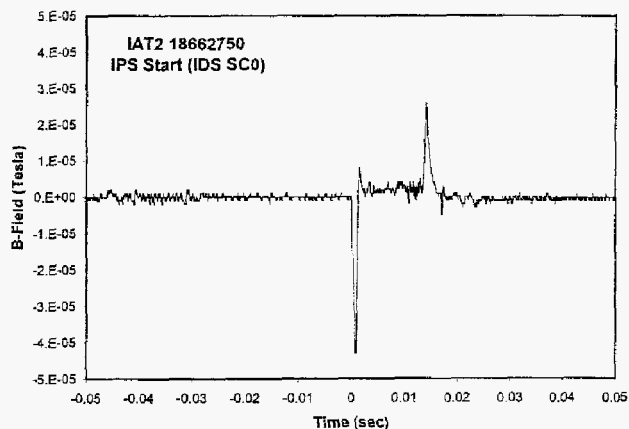


Figure 39. B-Field transient signal for flight IPS ignition

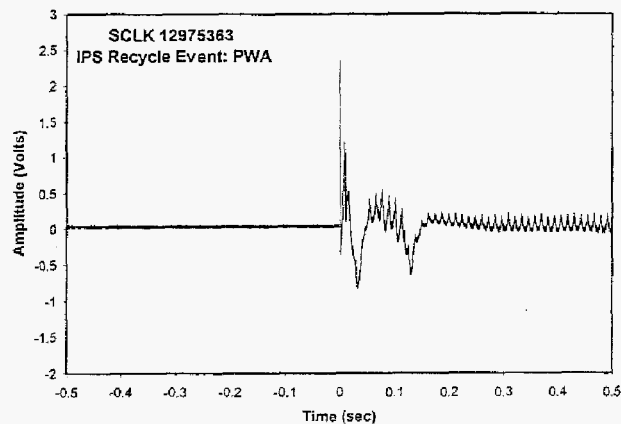


Figure 40. E-field signature for IPS recycle at $t=0$

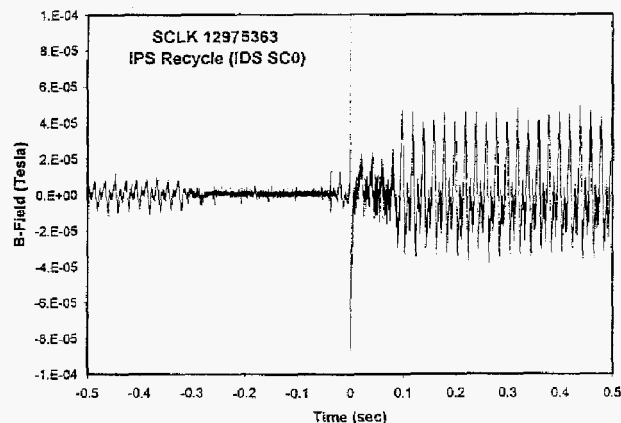


Figure 41. B-field signature for IPS recycle at $t=0$ (The large signals from $t=0.1$ to 0.5 are from gimbal actuators.)

Notice that the IPS starts at $t=0$ seconds and low frequency electric field oscillations continue to the end of the recording. The magnetic oscillations between $t=0.1$ and $t=0.5$ are due to the engine gimbal assembly motors.

The DS1 reaction control system (RCS) thrusters are responsible for some of the largest amplitude-transient signals observed by the IDS. As shown in Figures 42, and 43, the RCS-produced signals are substantial. Electric-field amplitudes in excess of $2 \text{ V}_{p-p}/\text{m}$ are typically observed for the RCS thruster firings. The origin of the high-amplitude E-field signal is not fully understood; however, a strong candidate is the ability of low-density gas flows to discharge electrically charged surfaces. The plasma wave antenna will become moderately charged due to the photoelectric effect. Some variation of the E-field amplitude has been observed with changes in Sun angle on DS1, supporting the possibility that charge dissipation is responsible for the signals. The magnetic field signals in Figure 43 are attributed to the solenoid valve-drive pulses. The various thruster firing combinations on DS1 yield unique, but reproducible, magnetic-field signatures. The magnetic field signature typically begins approximately 15 msec prior to the electric field signal in RCS thruster firings.

On several occasions, strong E-field transient events have been recorded by the IDS without RCS or IPS operations. These E-field signals do not have a simultaneous magnetic signature, suggesting a momentary plasma discharge. Such events have been attributed to hypervelocity impacts and have been observed in prior space missions (for example, Voyager). Figures 44 and 45 provide an example of such an event on DS1.

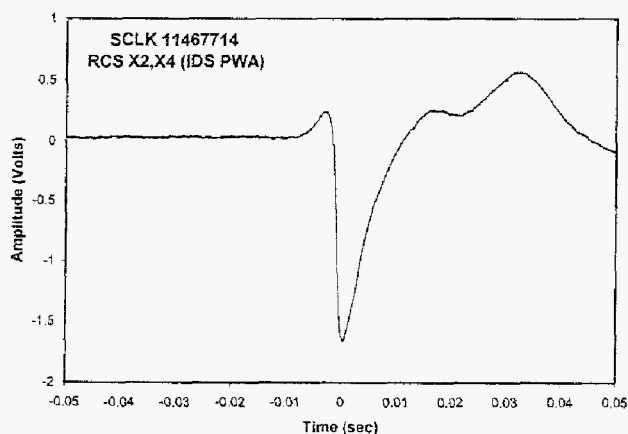


Figure 42. E-field signature for RCS thrusters firing at $t=0$

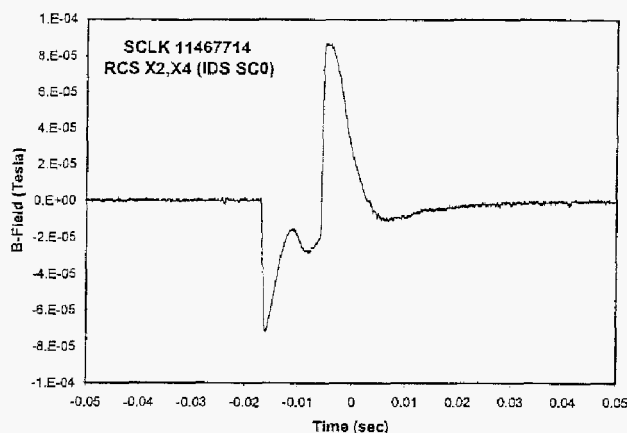


Figure 43. B-field signature for RCS thrusters firing at $t=0$

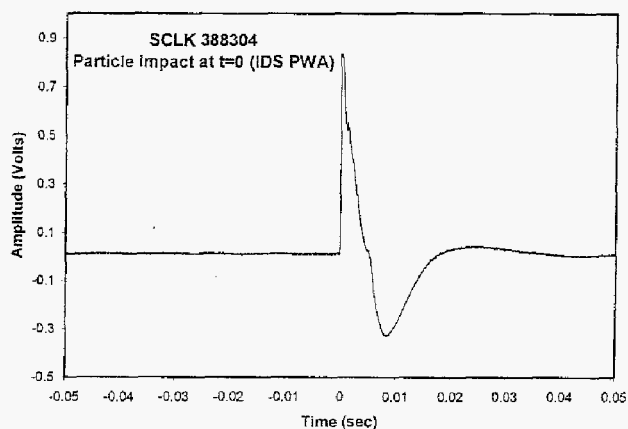


Figure 44. E-field signature for particle impact at $t=0$

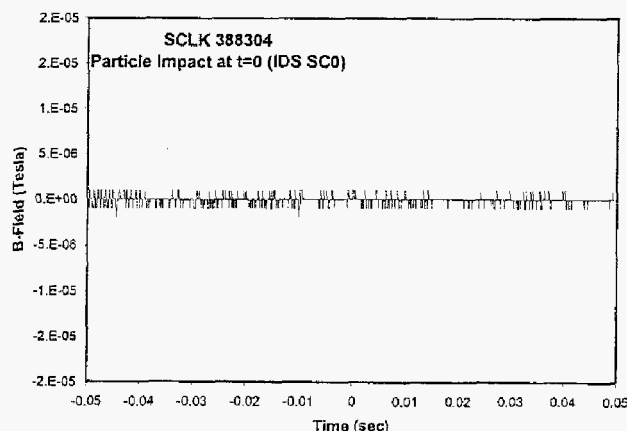


Figure 45. B-field recording for particle impact at $t=0$

IPS DC-MAGNETIC FIELDS

Ground Magnetic Field Mapping

The NSTAR ion engine includes strong permanent magnets arranged in a "ring-cusp" geometry to enhance the ionization efficiency within the discharge chamber⁸. These rare-earth permanent magnets are fabricated from samarium-cobalt ($\text{Sm}_2\text{Co}_{17}$) and have been thermally conditioned to improve their long-term stability. An important issue regarding the IPS permanent magnets is the stability of the fields during the lifetime of a science mission. The magnets are known to exhibit temperature-dependent changes in field strength; this dependence can be accurately determined prior to launch. The long-term stability of the temperature-compensated magnetic field characteristics is a critical factor for determining the compatibility of IPS with magnetic field science measurements during a mission.

A simple finite-element magnetic field model for the NSTAR ion engine was constructed using the student version of Q-Field (Tera Analysis). The configuration of the magnets permitted a simple, axial-symmetric model to be constructed. The location and pole orientation for the magnets were determined from NSTAR assembly drawings. The magnetic properties of the $\text{Sm}_2\text{Co}_{17}$ were obtained from the supplier literature. Figure 46 illustrates the magnetic flux density with a color scale and magnetic field lines at contour intervals of 500,000 nT. An outline for the NSTAR ion-engine shell is provided in the figure for clarity. There is a large external field lobe opposite from the ion-beam direction. The internal "ring-cusp" field lines are evident within the discharge chamber region. The upper bound for the field magnitudes for the IDS FGM sensors is approximately 11,000 nT for the inboard sensor and 3,200 nT for the outboard sensor.

The initial assessment of IPS magnetic fields and the long-term stability was performed in conjunction with the NSTAR 8000-hour life demonstration test (LDT) performed with an engineering model thruster (EMT#2). Prior to the start of the LDT, EMT#2 was characterized in the JPL Magnetic Mapping facility. As expected, very strong magnetic fields were observed in the mapping operation. A polar plot of the IPS magnetic is shown in Figure 47. This plot is overlaid upon a cross-sectional view of the IPS thruster. (Note that the orientation of the engine is reversed in Figures 45 and 46). The peak field, at a 1-meter distance from the approximate center of the IPS, was found to be 12,000 nT along the thruster centerline. Smaller field lobes were found roughly perpendicular to the thrust axis. This external-field geometry is consistent with the configuration and orientation of the magnets within the thruster assembly. The slight tilt of the lobes perpendicular to the thruster centerline is due to an offset of the engine magnetic "center" from the axis of the rotation table in the magnetic mapping

facility. Based on the EMT measurements, the predicted field magnitude for the IDS FGM sensors was about 7000 nT for the inboard sensor and 2800 nT for the outboard sensor. The variance from the magnetic model is due primarily to the effects of the thermal conditioning on the $\text{Sm}_2\text{Co}_{17}$ magnetics.

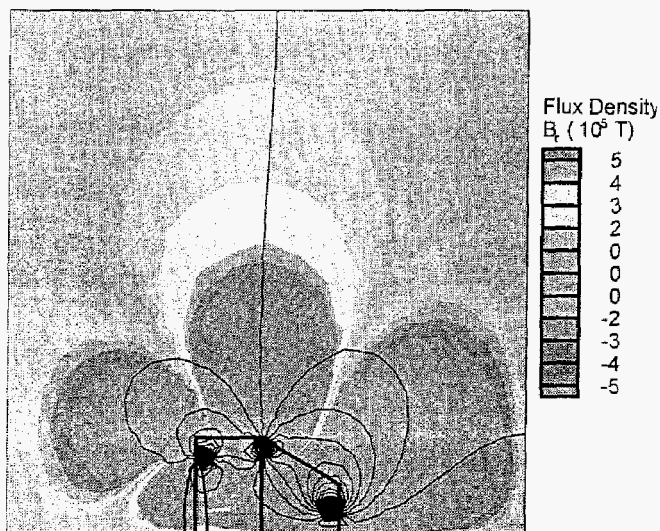


Figure 46. DC magnetic field model for the NSTAR ion engine

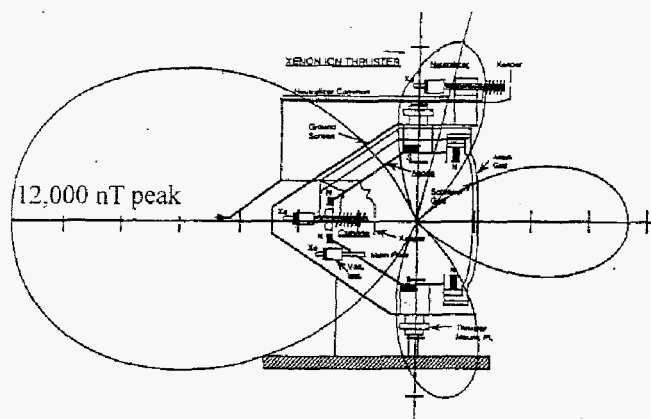


Figure 47. Pre-LDT magnetic map of the EMT#2 thruster

Subsequent to the completion of the 8000-hour LDT, the EMT#2 ion thruster was returned to the JPL Magnetic mapping facility. Since permanent fixtures for precisely positioning the IPS engine and magnetometer sensors within the magnetic mapping were not available, the mapping configuration was reconstructed based on photographic documentation of the pre-LDT set-up. The post-LDT mapping data were found to repeat the original results (within the ability to accurately re-create the pre-LDT mapping configuration). The estimated limit of magnetic strength degradation for the 8000-hour test is less than 5%.

The thermally-conditioned permanent $\text{Sm}_2\text{Co}_{17}$ magnets used in the NSTAR ion engine demonstrate stable magnetic characteristics after long-term operation at full power.

Flight Measurements

The following describes some long-term investigations on the DS1 FGM data. There is a list of interesting questions concerning the behavior of the ion engine permanent magnetics with respect to the FGM data.

- (1) Does the temperature play a significant role in the magnetic measurements?
- (21) If there is a temperature dependency, is it possible to make a model for temperature correction on the data?
- (3) Do the magnetic moments of the ion engine magnets vary with the time?

The following results are based on data transmitted to the TU-Braunschweig from launch to DOY 077-1999. Therefore, only the first six months of the mission is covered by this analysis. For the day of the encounter of DS1 at Braille, limited data are available (DOY 209/210-1999).

When the data are shown versus time, the x-axis is shown in units of day of the year 1999. Thus the days in 1998 are handled as "negative days." The magnetic and temperature data on the y-axis is the average of the specific data over the period of the assigned day (24-hour average).

Investigation of the Mean Residual Field—The plots in Figure 48 show the 24-hour averaged FGM data of the

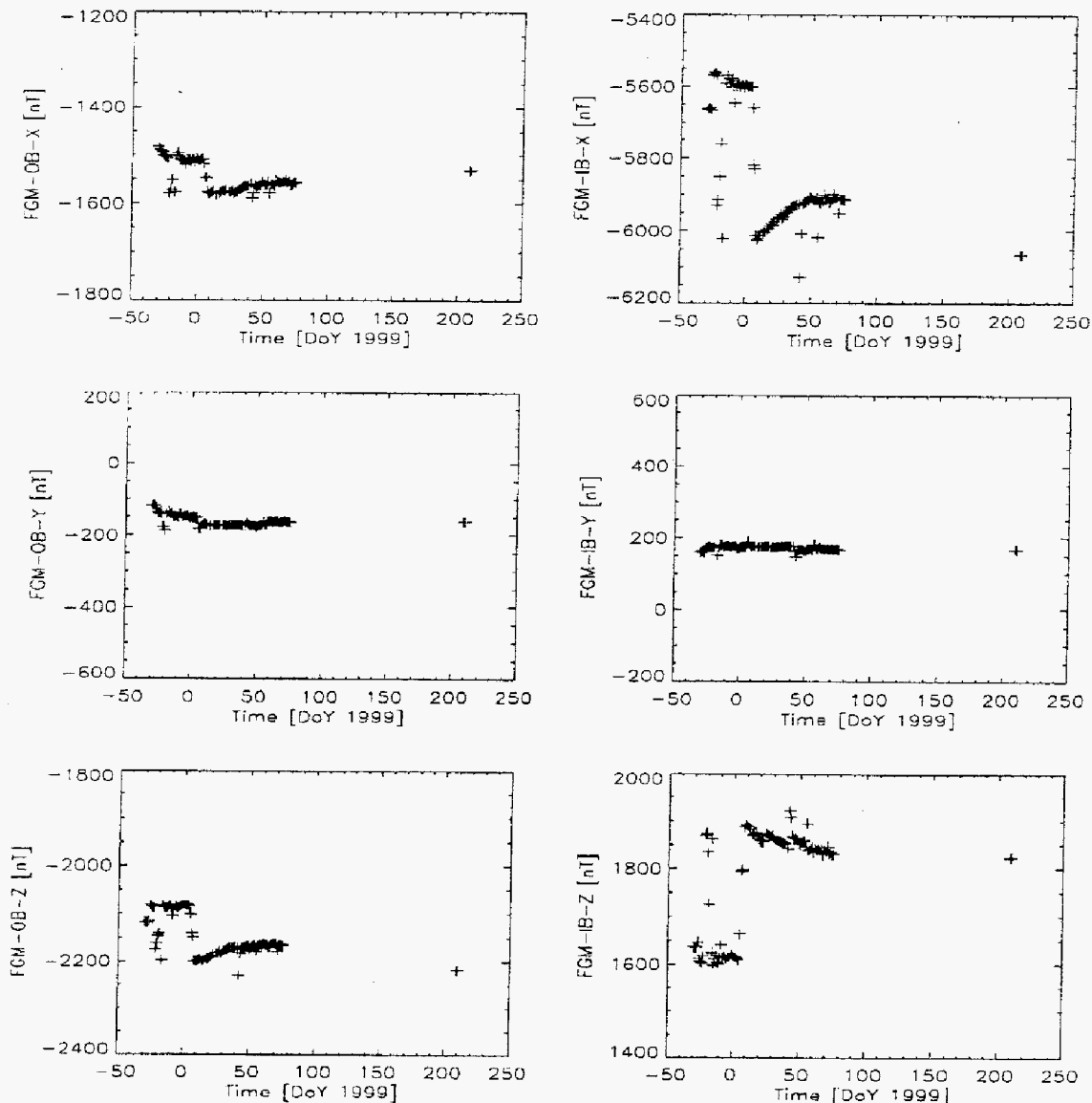


Figure 48. The 24-hour averaged, calibrated FGM data in DS1 coordinates

outboard (left column) magnetometer and the inboard (right column) magnetometer. The data are calibrated and displayed in spacecraft coordinates.

The ambient field of interplanetary space is in the order of a few nanotesla; the offsets of the magnetometers are also in the order of a few nanotesla. Therefore, it is quite obvious that the resulting huge magnetometer readings are caused by the spacecraft. The data show a strong variation over the time, especially in the x and z components. The inboard sensor (FGM-IB) shows larger absolute values and higher variations. These field variations are caused by the IPS permanent magnets. It is a known fact that the magnetic moment of a probe is strongly temperature dependent. Therefore, the next step is to look at the various temperature sensors on board DS1.

Figure 49 shows the data of four temperature sensors:

- T_INT refers to the internal ion-engine temperature sensor (IPS_THR_TMP).
- T_EXT refers to the external ion-engine temperature sensor (IPSTHRMSKTMP).

- T_FGM_IB refers to the inboard magnetometer temperature sensor.
- T_FGM_OB refers to the outboard magnetometer temperature sensor.

All the sensors show nearly the same structure; however, the sensors show different absolute values and different amounts of variation. At the beginning of the mission high temperatures are indicated. This corresponds to the operating ion engine. The engine was switched off on January 5, 1999. The sudden temperature decrease is easily seen in the data. The operating ion engine causes a higher temperature on the outboard sensor than on the inboard sensor. This might be due to the fact that the outboard sensor is placed a little bit nearer to the ion beam regime than the inboard sensor. The temperature measured inside the propulsion system decreases by about 150 °C when the engine is deactivated. In the following time, the system seems to be heated up exponentially. This is probably caused by gradual change in solar flux on the engine.

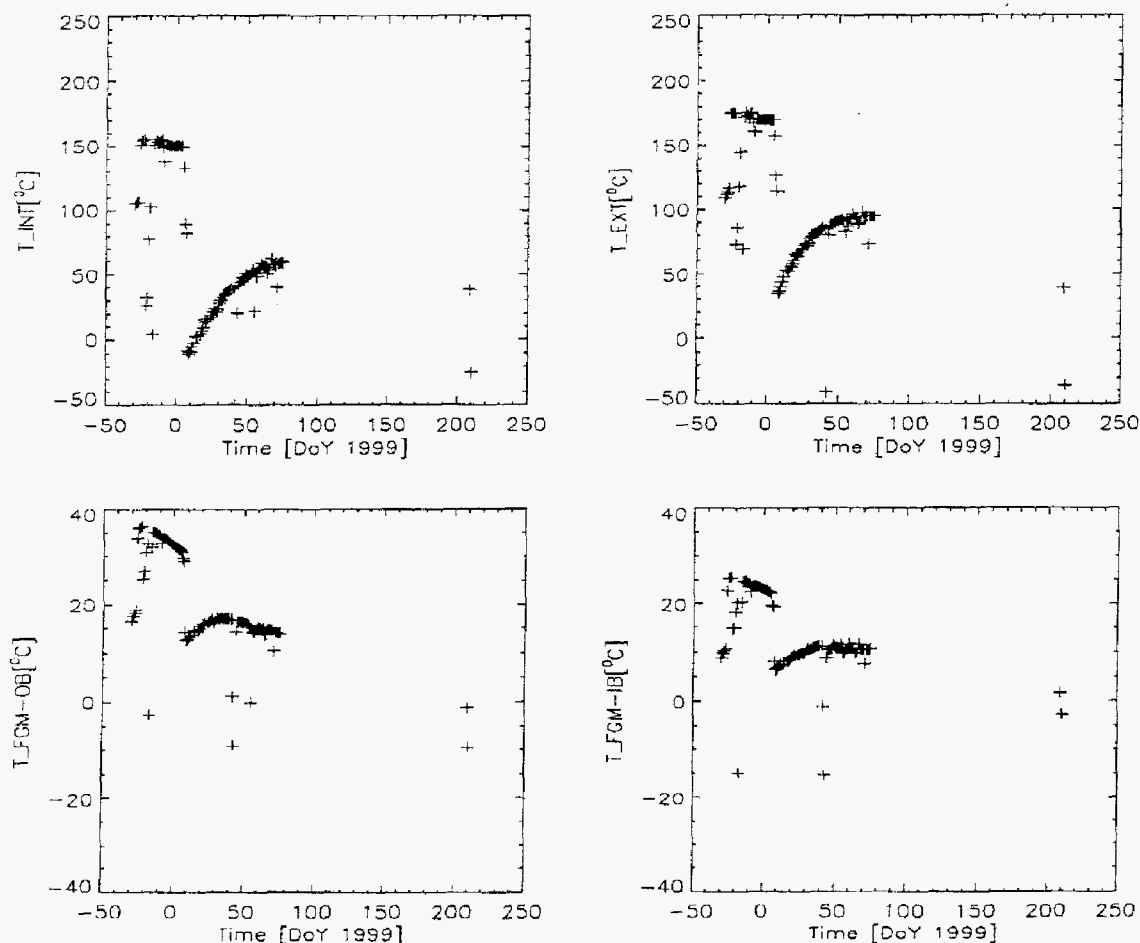


Figure 49. The 24-hour averaged temperature data from IPS thruster and FGM sensors

The comparison between the FGM magnetic field data and the measured temperatures suggests a linear model of the temperature dependence of the magnetic moments of the ion engine permanent magnets.

The best fit of such a model is shown in Figure 50. The intercept and slopes for the best fit for each component are printed above each plot. All components of the measured

magnetic field data show a linear dependency of the internal temperature T_{INT} . The x and z components show huge temperature variations. This is due to the geometric orientation of the magnetometer on the boom relative to the engine magnets. At 0 °C, the inboard FGM is in a 6315-nT field, whereas the outboard FGM is in a 2710-nT field.

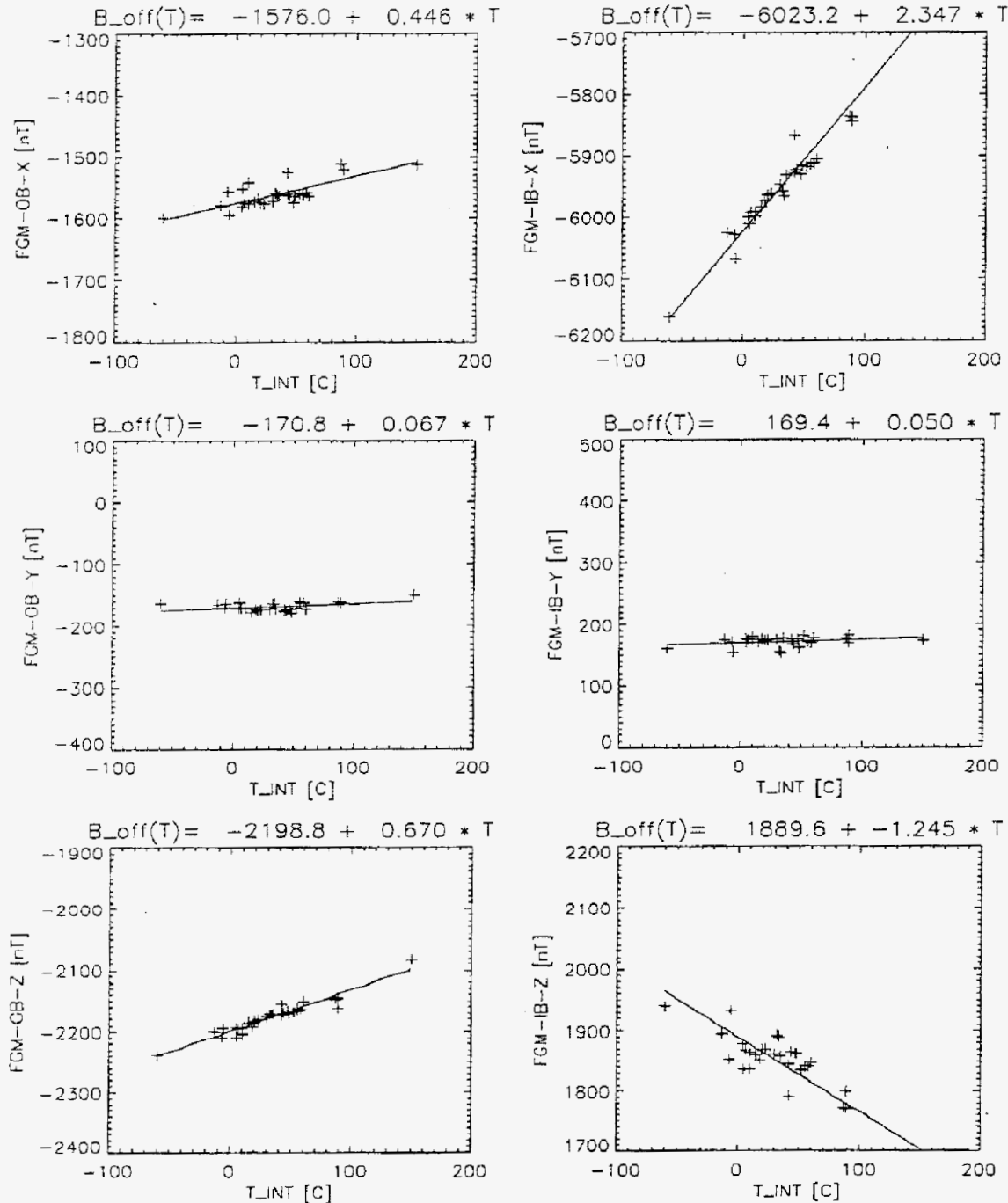


Figure 50. The linear temperature model of the IPS thruster magnetic field

The application of this model to the data leads to linear-temperature-corrected magnetic-field data, shown in Figure 51. The strong temperature dependence is diminished and the resulting residual field is suppressed. However, the model is not completely perfect. Especially on the x and z components of the FGM-IB magnetometer, which is located near the magnet, some linear (in the time domain, not in the temperature domain!) trend remains. This could be caused

by a temporal variation of the magnets themselves. Further investigation is required to resolve the magnetic stability.

A further cross check of the temperature model is given by investigation of the engine-temperature-corrected data versus the FGM sensor temperatures. These data are shown in Figure 52.

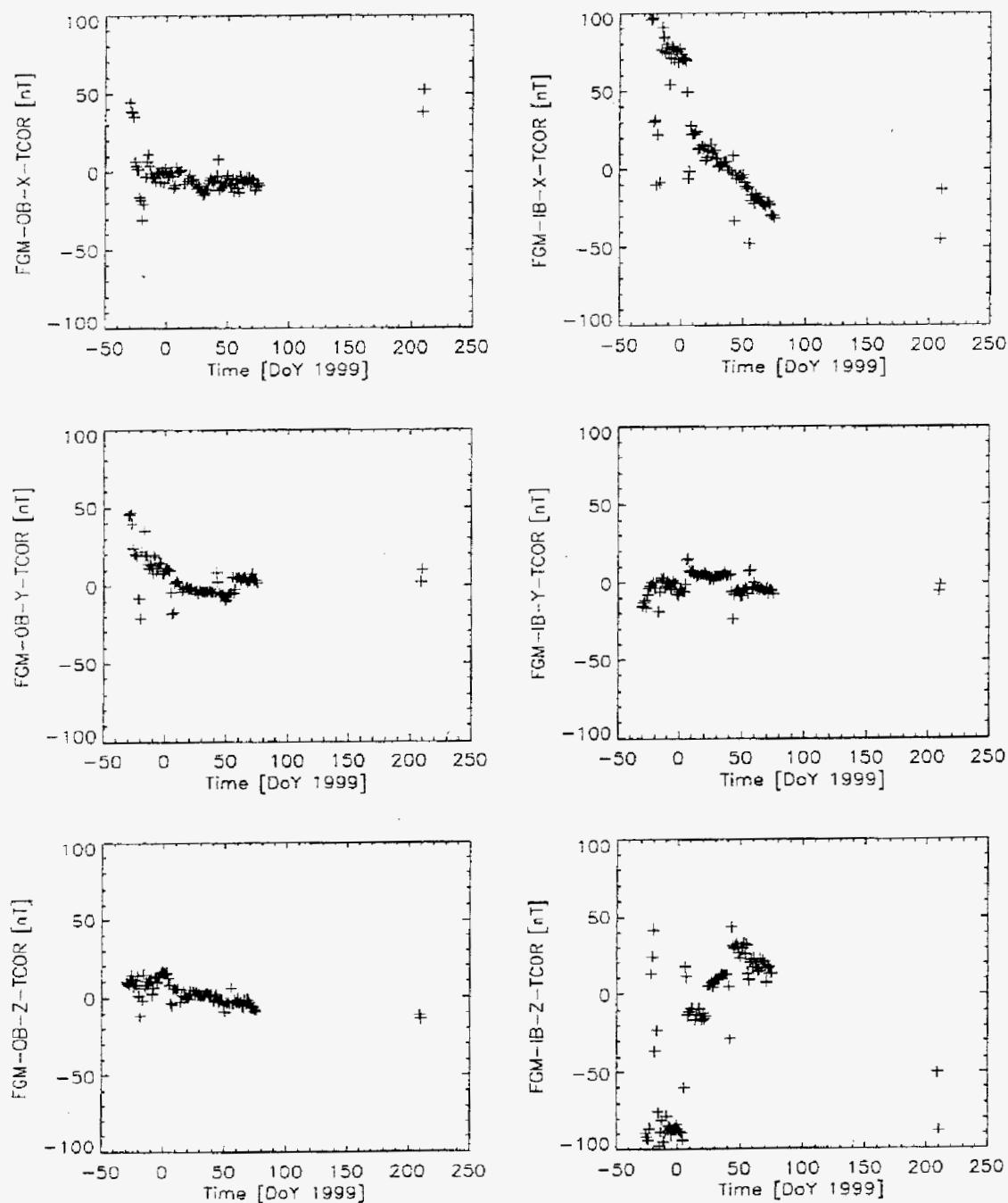


Figure 51. Residual magnetic field data after temperature correction

The plots show that there is almost no temperature dependence to be seen. The data are straying nearly

randomly. This means that the temperature model does include the temperature-caused effects sufficiently.

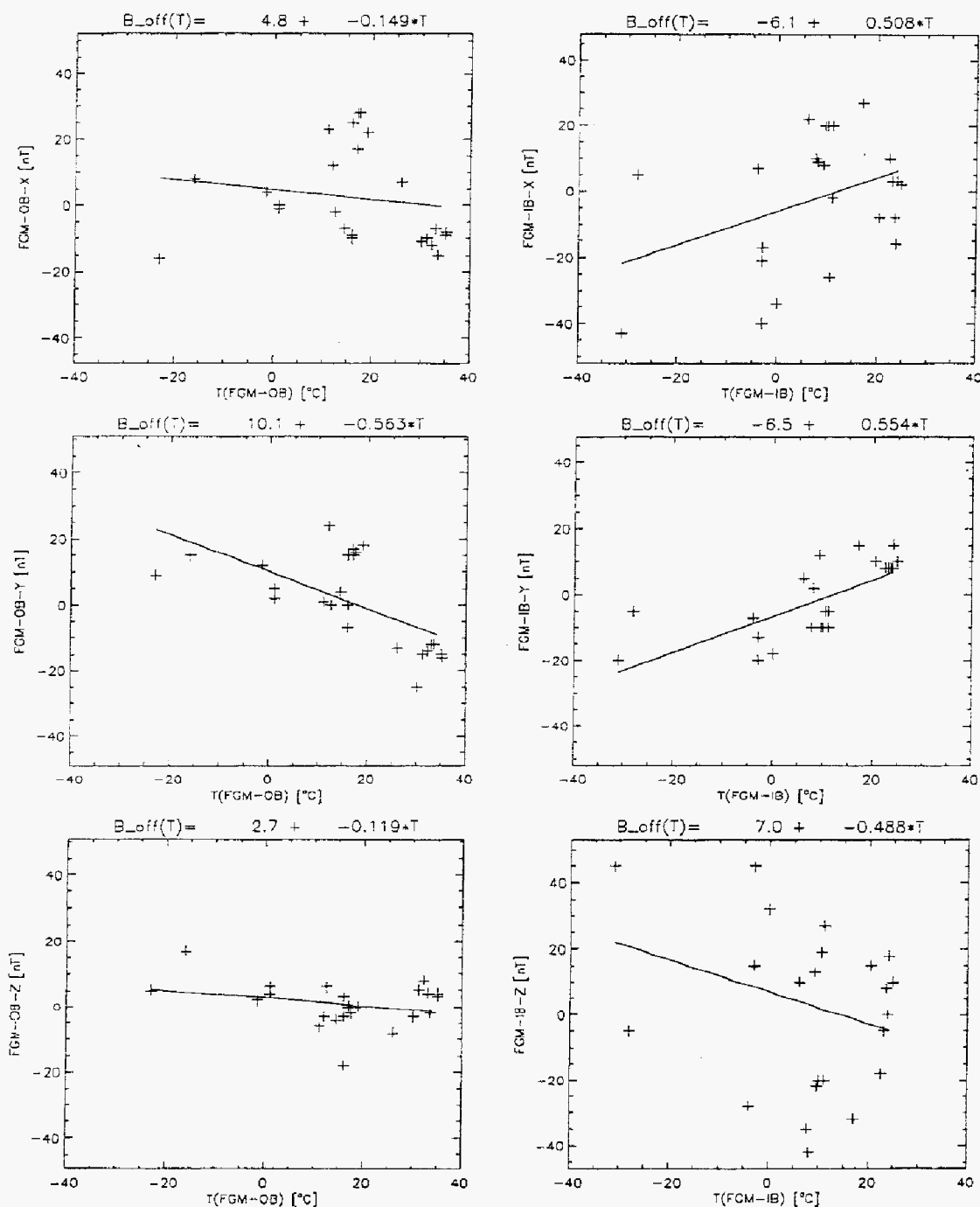


Figure 52. Temperature-corrected FGM field data versus FGM temperature

CONCLUSIONS

DS1 provided an excellent opportunity for in-depth investigation of interactions of an ion propulsion system with an interplanetary spacecraft in flight. The NSTAR project recognized the importance of characterizing the local environment due to IPS operations and chose to fly a diverse set of instrumentation. The sensors were selected to capture the range of expected signals from the IPS. Hence, the sensor sensitivity and response characteristics are generally less than what is found in space-science instrumentation. Notable exceptions to the above statement are the flux-gate magnetometers provided by the Technical University of Braunschweig. The FGMs have performed exceptionally well throughout the mission and may have detected a weak (2 nT) magnetic signature during the flyby of Asteroid Braille²³. The IDS has succeeded in collecting the data required to characterize the local environment and effects induced by the IPS operating on DS1.

Analysis of the IDS measurements of ion energies and densities and electron temperatures have validated sophisticated numerical-simulation models of the charge-exchange plasma produced by the IPS. Although a wider Langmuir-probe voltage-sweep range would have permitted independent electron density determination, the Langmuir probe performance was sufficient to obtain electron temperature data. Ion-current measurements from the retarding-potential analyzer allowed the charge-exchange density to be determined. The IPS charge-exchange plasma induced a shift of the DS1 spacecraft potential by -6 V to -10 V with respect to ambient "space ground." In ground testing, the spacecraft was tied to Earth ground, as were the walls of the vacuum facility. A peak plasma potential of 5 to 7 V was observed in ground test, whereas the peak plasma potential exceeded 15 V with respect to spacecraft ground in flight. In terms of effects of the charge exchange on spacecraft subsystems, no degradation of the spacecraft power system due to parasitic current collection by the SCARLET solar arrays was observed during IPS operations. PEPE detected a substantial flux of charge-exchange xenon ions without effecting measurements of solar wind protons. The effects of IPS operations on PEPE solar wind electrons are still being evaluated.

The IDS contamination monitors returned high-quality measurements of deposition of IPS grid-erosion products during the DS1 mission. The line-of-sight quartz crystal microbalance accumulated 35 nm of molybdenum after 7300 hours of IPS operation. The line-of-sight accumulation is consistent with deposition observed during the 8000-hour LDT. The amount of non-line-of-sight molybdenum accumulation (3.5 nm after 7300 hours) is higher than the pre-flight prediction of <0.5 nm. Non-line-of-sight deposition is due to surface accumulation of molybdenum ions, whose trajectories are deflected by local electrostatic

fields on DS1. The pre-flight estimate of molybdenum ion production did not include the possibility of charge-exchange between neutral molybdenum and beam ions. Subsequent communication²² revealed the Mo-Xe⁺ cross-section is surprisingly large; this channel dominates in the formation of molybdenum ions. Non-line-of-sight contamination measurements in ground test are not feasible due to interference from material sputtered from chamber walls. Flight measurements are the only reliable source for assessing non-line-of-sight deposition from the IPS engine on DS1.

The IDS Plasma Wave Spectrometer characterized the electrostatic wave and electromagnetic noise environments produced by the IPS and other DS1 subsystems. A large volume of both spectral and time-domain data were obtained throughout the DS1 mission, especially during IPS operations. There is not a direct correlation of noise amplitude with IPS operating power. The IPS noise levels are bounded as follows:

- IPS E-field continuous noise: < 1 V/m, < 15 MHz.
- IPS E-field transient: < 2 V/m for < 1 ms.
- IPS B-field continuous noise: < 10 μ T, < 10 kHz.
- IPS B-field transient: < 200 μ T for < 2 ms.

Limits for the major DS1 subsystem noise sources, namely the hydrazine reaction control subsystem (RCS) thrusters and engine gimbal actuators (EGAs), are bounded by:

- RCS thruster E-field transient: < 5 V/m for < 10 ms.
- RCS thruster B-field transient: < 200 μ T for < 40 ms.
- EGA B-field continuous noise: < 10 μ T, at 100 Hz.
- EGA B-field transient: < 100 μ T for < 1 s.

From a spacecraft systems-engineering perspective, the IPS does not produce *peak* electromagnetic or electrostatic noise beyond that of other spacecraft subsystems¹⁵. Note that, when operating, the IPS produces noise continuously; conversely, the other spacecraft sources are typically transient in nature. A major finding is the IPS does not introduce any interference in spacecraft communications or other subsystem operations.

The presence of high-strength permanent magnets within the IPS is a concern for performing magnetic-science measurements. The opportunity for science measurements is improved if the IPS permanent magnetic field can be accurately characterized and removed as background from the science measurement. For high-sensitivity magnetometers, it is important to locate the sensors as far as possible from the IPS and have accurate knowledge of the geometric orientation and temperature-compensated magnetic fields. Long-term degradation of the magnets can introduce significant errors in this approach to removing the

background field. The IDS FGM sensors provided in-flight temperature-compensation data for and demonstrated the long-term stability of the IPS magnets. The use of dual FGM sensors and principal component-analysis technique led to the possible detection of a weak magnetic signature at Asteroid Braille²³, demonstrating the potential for performing magnetic science even in the presence of large, local magnetic fields.

ACKNOWLEDGMENTS

The research described in this paper was carried out at the Jet Propulsion Laboratory, California Institute of Technology, under a contract with the National Aeronautics and Space Administration.

Reference herein to any specific commercial product, process, or service by trade name, trademark, manufacturer, or otherwise, does not constitute or imply its endorsement by the United States Government, or the Jet Propulsion Laboratory, California Institute of Technology.

The IDS development effort was primarily funded by the NSTAR Project under the management of John F. Stocky, who provided valuable advice as well a programmatic support. The support of the NSTAR Project Office, especially from Michael Marcucci, Jim Tribbett, and Henrik Gronroos, is deeply appreciated. The ground-test portion of this effort was made possible by the following JPL personnel: John Brophy, Jay Polk, Keith Goodfellow, Pablo Narvaez, and John Anderson. Additional IDS development support was provided by members of the Integrated Space Physics Instrument team, including the following individuals not included in the author list: Kim Leschley, Gerry Murphy, and Gregg Vane. The following individuals at Physical Sciences, Inc. contributed substantially to the DSEU hardware and software development: Prakash Joshi, B. David Green, George Caledonia, Eric Lund, Michael Hinds, and Brian Root. Valuable hardware fabrication and test support was received from Chris Coles at Sentran Corp. Key personnel supporting fabrication and assembly of the IDS at JPL include Dave Rooney, John Bousman, Michael Parks, Michael O'Connell, and Greg Hickey.

The Deep Space 1 spacecraft team provided substantial assistance in the development, integration, and test of the IDS hardware. The authors appreciate the extra effort from the following individuals: Leslie Livesay, Gaylon McSmith, J. Sean Howard, Gary Glass, and Andy Rose. The New Millennium Program Chief Scientist, David Crisp, provided crucial support in obtaining approvals for the TUB hardware contribution. The DS1 Mission Operations and Deep Space Network teams supported the IDS operations phase with much appreciated extra effort from Marc Rayman, Phil Varghese, Bud Ford, Hank Hotz, Robert Gounley, Curt Eggemeyer, Kathy Moyd, and Tom Boreham.

Important hardware contributions to the IDS were made by the Institute for Geophysics and Meteorology of the Technical University of Braunschweig (TUB) and TRW. TUB provided the flux-gate magnetometers with signal processing electronics. TRW provided the plasma-wave spectrometer electronics and the plasma wave pre-amplifier. These contributions made possible the important electric and magnetic fields measurements obtained by IDS and substantially augmented the validation of ion propulsion on DS1.

The work by Guenter Musmann, Falko Kuhnke, Ingo Richter, Carsten Othmer, and Karl-Heinz Glassmeier was financially supported by the German Bundesministerium fuer Bildung und Forschung and the Deutsches Zentrum fuer Luft- und Raumfahrt under contract 50 OO 99037.

REFERENCES

- [1] D. Brinza, editor, Report on the NASA/USAF Workshop on Environmental Diagnostics for ELITE/STAR, *JPL D-11595*, 1994.
- [2] M.R. Carruth, A review of studies on ion thruster beam and charge-exchange plasmas, *AIAA Paper 82-1994*, 1982.
- [3] I. Katz, V. Davis, J. Wang and D. Brinza, Electrical potentials in the NSTAR charge-exchange plume, *IEPC Paper 97-042*, 1997.
- [4] I. Katz, D.E. Parks, M.J. Mandell and G.W. Schnuelle, Parasitic current losses due to solar-electric propulsion generated plasmas, *J. Spacecraft and Rockets*, 19(2), 129, 1982.
- [5] J.R. Brophy, J.E. Polk and L.C. Pless, Test-to-failure of a two-grid, 30-cm-dia. ion accelerator system, *IEPC Paper 93-172*, 1993.
- [6] G. Jongeward, M.J. Mandell, I. Katz, B. Bucholtz, S. Snyder and P. Wilbur, Conductive Nature of Low Frequency (<1 MHz) Electromagnetic Fields Generated by a Hollow Cathode Plasma Contactor, *AIAA Paper 94-3313*, 1994.
- [7] J.D. Huba, NRL Plasma Formulary, Revised 1998, Naval Research Laboratory, *NRL/PU/6790-98-358*, 28, 1998.
- [8] M.J. Patterson, Performance characteristics of ring-cusp thrusters with xenon propellant, *AIAA Paper 86-1392*, 1986.

- [9] J.A. Christensen, K.J. Freick, D.J. Hamel, S.L. Hart, K.T. Norenberg, T.W. Haag, M.J. Patterson, V.K. Rawlin, J.S. Sovey and J.R. Anderson, Design and fabrication of a flight model 2.3 kW ion thruster for the Deep Space 1 Mission, *AIAA Paper 98-3327*, 1998.
- [10] J.E. Polk, J.R. Anderson, J.R. Brophy, V.K. Rawlin, M.J. Patterson, J. Sovey and J. Hamley, An overview of the results from an 8200 hour wear test of the NSTAR ion thruster, *AIAA Paper 99-2446*, 1999.
- [11] J.J. Wang, D.E. Brinza and M. Young, Three-dimensional particle simulation modeling of ion propulsion plasma environment for Deep Space 1, submitted to *J. Spacecraft and Rockets*, 2000.
- [12] V. Davis, I. Katz, M. Mandell, D. Brinza, M. Henry, J. Wang and D. Young, Ion engine generated charge-exchange environment, comparison between NSTAR flight data and numerical simulations, *AIAA Paper 2000-3529*, 2000.
- [13] G.S. Arnold, D.E. Brinza, P. Joshi, D.N. Keener, Space active modular materials experiment, *SPIE Proc. Vol. 3427*, 225, 1998.
- [14] P. Joshi, M. Malonson, B.D. Green, J. McKay, D.E. Brinza and G.S. Arnold, Space Environment and Effect Monitoring Instrumentation for Small Satellites, *J. Spacecraft and Rockets*, 35(6), 821, 1998.
- [15] M.D. Henry, D.E. Brinza, A.T. Mactutis, K.P. McCarty, J.D. Rademacher, T.R. vanZandt, R. Johnson, G. Musmann and F. Kunke, NSTAR Diagnostics Package Architecture and Deep Space One Spacecraft Event Detection, *IEEE 2000 Aerospace Conference Paper 11.0502*, 2000.
- [16] D.A. Wallace and S.A. Wallace, Realistic performance specifications for flight quartz crystal microbalance instruments for contamination measurement on spacecraft, *AIAA Paper 88-2727*, 1988.
- [17] P.J. Reichardt and J.J. Triolo, Preflight testing of the ATS-1 thermal coatings experiment, *Thermophysics of Spacecraft and Planetary Bodies. Progress in Astronautics and Aeronautics, Vol. 20*, Academic Press, 1967.
- [18] E.B. Hurst and G.Z. Thomas, Diagnostic system design for the ion auxiliary propulsion system (IAPS) – Flight test of two 8 cm mercury ion, *NASA Technical Memorandum 81702*, 1981.
- [19] S. Sakabe. and Y. Izawa, Simple formula for the cross sections of resonant charge transfer between atoms and their positive ions at low impact velocity, *Phys Rev A*, 45(3), 2086, 1992.
- [20] J.E. Polk, J.R. Brophy and J. Wang, Spatial and temporal distribution of ion engine accelerator grid erosion, *AIAA Paper 95-2924*, 1995.
- [21] D.E. Brinza, J. Wang, J.E. Polk, and M.D. Henry, Deep Space One Measurements of Ion Propulsion Contamination, accepted to *J. Spacecraft and Rockets*, 2000.
- [22] Private communication with Rainer Dressler, AFRL/VSBS.
- [23] I. Richter, C. Othmer, F. Kuhnke, K.-H. Glassmeier, D. Brinza and B. Tsurutani, Magnetometer observations during the fly-by of the Deep Space 1 spacecraft at the Asteroid Braille, *GP31A-09*, 2000 American Geophysical Union Spring Meeting, Washington D.C., 2000.

APPENDIX A. DETAILED IDS QCM HISTORY FOR THE FIRST YEAR OF FLIGHT BY DS1

The first period of extended IPS operations occurred from DOY 328-1998 to DOY 005-1999. The line-of-sight sensor (QCM0) response is shown in Figures A.1a and A.1c; the shadowed-sensor (QCM1) response is seen in Figures A.1b and A.1d. The initial IPS operations consisted of 10 days thrusting with the thrust vector essentially Earth-pointed. During these initial operations, the NSTAR engine was first operated at low-thrust (mission levels 6 to 27) for five days. During this period, QCM0 frequency increased by 123 Hz, while QCM1 increased by 25 Hz. To determine the deposition rates for mission level 27 (ML27), least squares fits of the frequency data for the 117-hour interval starting on DOY 329-1998 and ending on DOY 334 were performed. The resulting slope in units of Hz/day was converted to $\text{\AA}(\text{Mo})/\text{kHr}$ by multiplying by 1.804.

QCM0 data for the remaining thrusting of the initial period shows some interesting features. On DOY 338-1998, DS1 performed a turn to orient the thrust vector from Earth-pointed to the desired mission trajectory thrust attitude. In this turn, the solar illumination of the thruster increased from grazing (80° off of the thrust axis) to about 0.77 suns (40° off of the thrust axis). Note that the molybdenum deposition rate for QCM0 at ML83 prior to DOY 338-1998 was $88 \text{ \AA}/\text{kHr}$, whereas after the turn, the deposition rate increased to $197 \text{ \AA}/\text{kHr}$. The accumulation rate of QCM1 almost doubles after the turn. It is not yet known whether this rate change is due to thermal effects on the NSTAR ion engine grids. There have been no reports of change in mass sensitivity with varying Sun angle on QCMs; therefore, it is unlikely that the rate change is an instrument artifact.

Following the turn to thrust attitude, DS1 continued thrusting until DOY 342-1998. Other technology activities, including initial turn-on of the Plasma Experiment for Planetary Exploration (PEPE) instrument were performed. On DOY 346-1998, IPS was restarted at low-thrust level (ML6) to assess the effects on the PEPE instrument. The on-board sequence raised the IPS thrust level to ML85 after 15 minutes. The available power for IPS thrusting was overestimated, resulting in a DS1 "safe-mode" transition. IPS thrusting resumed on DOY 348-1998 after DS1 spent two days in safe mode.

The first IPS thrust segment ended with two weeks of essentially continuous thrusting, with the thrust levels gradually decreasing from ML78 on DOY 352-1998 to ML 72 on DOY 005-1999. During this interval, the DS1 on-board navigation software would update the thrust vector and level at 12-hour intervals. The IPS thruster was turned off at 1600 hours on DOY 005-1999. The deposition on

QCM0 steadily increased over this interval, except for a brief interval on DOY 356-1998 where DS1 re-oriented to place the Sun on the X-axis for approximately 3 hours. QCM1 also showed consistent frequency increase, although at an order-of-magnitude lower than that for QCM0. The thrust segment continued into early 1999, with steady accumulation by both QCMs witnessed in Figures A.1c and A.1d. Subsequent to engine turn-off on DOY 005-1999, DS1 performed maneuvers to characterize stray-light into the MICAS imager. The effect of minor Sun-angle changes caused by attitude control system dead-banding on QCM1 (100 Hz amplitude oscillations) is quite evident for DOY 009-1999 through DOY 012-1999.

The next major IPS thrust interval was the C1A and C1B activities performed from DOY 075-1999 until DOY 117-1999. This thrusting was performed with weekly optical navigation (OpNav) activities and high-rate telemetry downlink intervals. The thrusting duty cycle was typically greater than 90% during this interval. The OpNav/downlink events are readily identified in Figures A.1d and A.1e by 100-Hz frequency dips in both QCM0 and QCM1 as well as 60°C temperature increases for both sensors. The deposition rates for QCM0 are labeled in Figure A.1d with time-averaged thruster mission levels for each thrust segment. During the C1A and C1B activities, the on-board navigator commanded the desired IPS mission level. The DS1 power management software would monitor battery state-of-charge and perform thrust reduction as required. For this period, the non-line-of-sight sensor (QCM1) accumulated only about 1% of the amount of molybdenum collected by QCM0. This value is consistent with pre-flight estimates for production and collection of ionized molybdenum from the thruster plume.

Subsequent to the Asteroid Braille encounter on DOY 210-1999, IPS operated for an interval of almost 12 weeks. As the DS1-Sun distance decreased, the mission level gradually increased during the C2A and C2B segments. The deposition rates of both QCMs also increased during this period, as seen in Figures A.1g and A.1h. The brief, periodic spikes in the QCM frequency data occur at each of the weekly OpNav and downlink sessions, again caused by Sun-angle changes. The accumulation of molybdenum on the shadowed QCM is about 5% of that witnessed by the line-of-sight sensor.

The four thrusting segments shown in Figures A.1a through A.1h account for more than 95% of the IPS operating time for the first year of the mission. Of the 250 \AA of molybdenum collected on the line-of-sight QCM in the first year of operation, almost 95% of the accumulation are shown in these figures. The shadowed QCM collected the equivalent mass of a 25-\AA thick deposit of molybdenum in the first year.

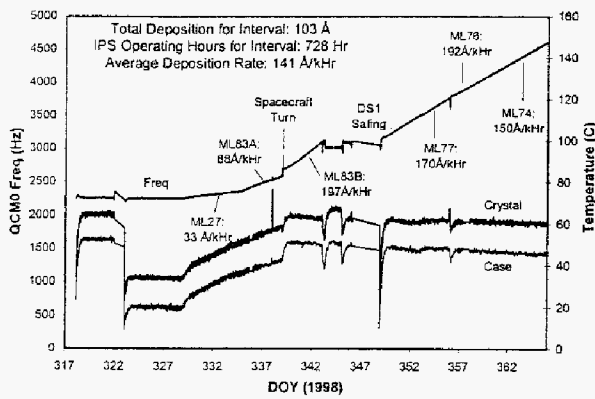


Figure A.1a. QCM0 Data for 1998-317 through 1998-365

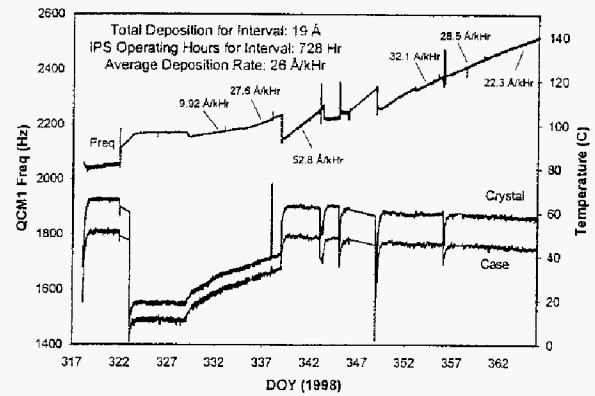


Figure A.1b. QCM1 Data for 1998-317 through 1998-365

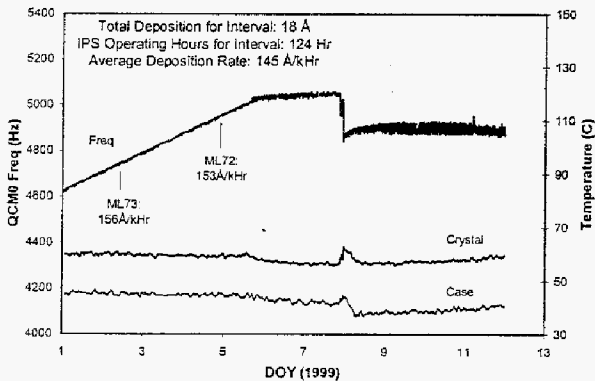


Figure A.1c. QCM0 Data for 1999-001 through 1999-012

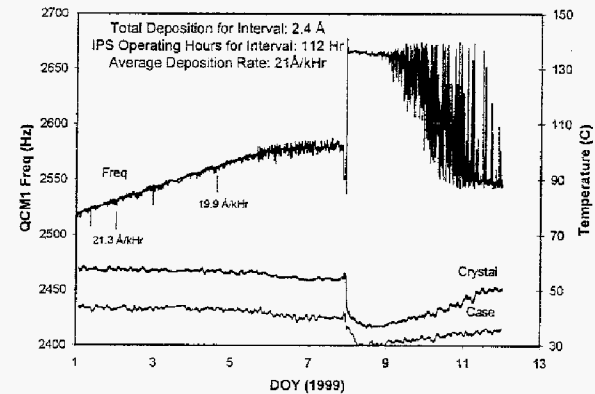


Figure A.1d. QCM1 Data for 1999-001 through 1999-012

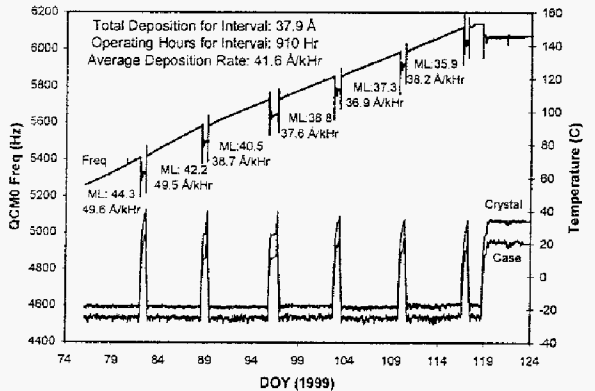


Figure A.1e. QCM0 Data for 1999-074 through 1999-124

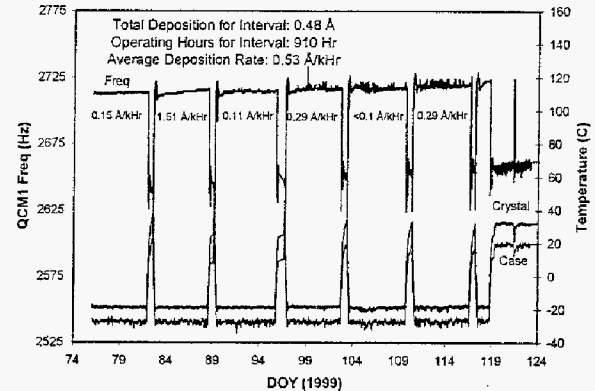


Figure A.1f. QCM1 Data for 1999-074 through 1999-124

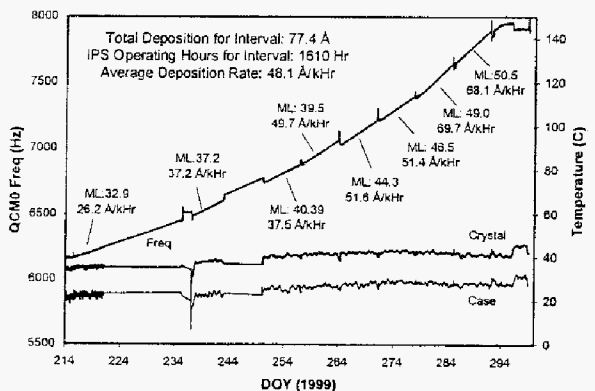


Figure A.1g. QCM0 Data for 1999-214 through 1999-300

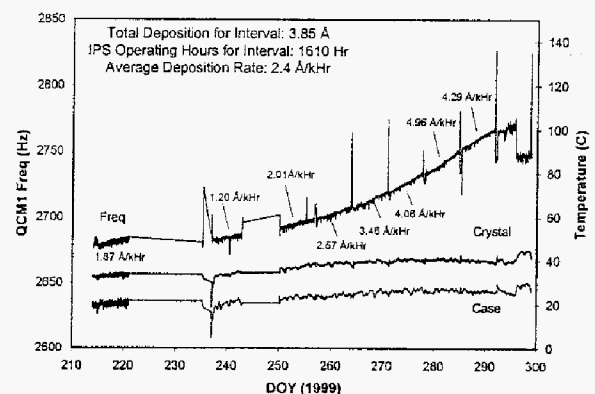


Figure A.1h. QCM1 Data for 1999-214 through 1999-300

APPENDIX B. LIST OF ACRONYMS AND ABBREVIATIONS

AC	Alternating Current	LPO	Langmuir Probe (spherical)
ACS	Attitude Control System	LP1	Langmuir Probe (planar ring)
AU	Astronomical Unit	MICAS	Miniature Integrated Camera and Spectrometer
CAL0	Calorimeter (Line-of-sight)	ML#	Mission Level (#)
CAL1	Calorimeter (Non-line-of-sight)	MLI	Multi-layer Insulation
CEX	Charge-exchange Xenon	NDP	NSTAR Diagnostics Package
DC	Direct Current	NSTAR	NASA SEP Technology Applications Readiness
DOY	Day-of-year	PCB	Printed Circuit Board
DS1	Deep Space One	PIC	Particle-in-cell
DSEU	Diagnostics Sensors Electronics Unit	PPU	Power Processor Unit
EGA	Engine Gimbal Assembly	PWA	Plasma Wave Antenna
EMC	Electromagnetic Compatibility	PWS	Plasma Wave Spectrometer
EMI	Electromagnetic Interference	QCM0	Quartz Crystal Microbalance (Line-of-sight)
EMT	Engineering Model Thruster	QCM1	Quartz Crystal Microbalance (non-line-of-sight)
eEV	Electron Volt	RCS	Reactive Control Subsystem
EWB	Environment Work Bench	RF	Radio Frequency
FGM_IB	Flux-Gate Magnetometer (Inboard)	RPA	Retarding Potential Analyzer
FGM_OB	Flux-Gate Magnetometer (Outboard)	RSU	Remote Sensors Unit
FMP	Fields Measurement Processor	SCM0	Search Coil Magnetometer (Miniature)
IAT1	IPS Acceptance Test #1	SCM1	Search Coil Magnetometer (Science, Inactive)
IAT2	IPS Acceptance Test #2	SEM	Scanning Electron Microscopy
IDS	IPS Diagnostics Subsystem	SEP	Solar Electric Propulsion
IPS	Ion Propulsion Subsystem	SMA	Shape-memory Alloy
LDT	Life Demonstration Test	TUB	Technical University of Braunschweig
LOS	Line-on-sight	VDC	Volts Direct Current